Nonlinear Dyn (2018) 92:1023–1043
https://doi.org/10.1007/s11071-018-4106-4

ORIGINAL PAPER

Detumbling strategy and coordination control of kinematically redundant space robot after capturing a tumbling target

Mingming Wang · Jianjun Luo · Jianping Yuan · Ulrich Walter

Received: 17 April 2017 / Accepted: 26 January 2018 / Published online: 7 February 2018

Abstract This paper focuses on the motion planning to detumble and control of a space robot to capture a non-cooperative target satellite. The objective is to construct a detumbling strategy for the target and a coordination control scheme for the space robotic system in post-capture phase. First, the dynamics of the kinematically redundant space robot after grasping the target is presented, which lays the foundation for the coordination controller design. Subsequently, optimal detumbling strategy for the post-capture phase is proposed based on the quartic Bézier curves and adaptive particle swarm optimization algorithm subject to the specific constraints. Both detumbling time and control torques were taken into account for the generation of the optimal detumbling strategy. Furthermore, a coordination control scheme is designed to track the designed reference path while regulating the attitude of the chaser to a desired value. The space robot successfully dumps the initial velocity of the tumbling satellite and controls the base attitude synchronously. Simulation results are presented for detumbling a target with rotational motion using a seven degree-of-freedom redundant space manipulator, which demonstrates the feasibility and effectiveness of the proposed method.

Keywords Detumbling strategy · Coordination control · Post-capture · Tumbling target

M. Wang · J. Luo (✉) · J. Yuan
Science and Technology on Aerospace Flight Dynamics Laboratory, Northwestern Polytechnical University, Xi'an 710072, China
e-mail: jjluo@nwpu.edu.cn

M. Wang · J. Luo · J. Yuan
Research Institute of Northwestern Polytechnical University in Shenzhen, Shenzhen 518057, China
e-mail: mwang@nwpu.edu.cn

J. Yuan
e-mail: jyuan@nwpu.edu.cn

U. Walter
Institute of Astronautics, Technical University of Munich, 85748 Garching, Germany
e-mail: walter@tum.de

1 Introduction

In light of the space robots currently planned by worldwide space agencies, an increase in the number and the capacity of robot applied in space missions will be a foregone conclusion in the coming future to fulfill the increasing demands of satellite maintenance, on-orbit assembly and space debris removal etc. [1–4]. One of the most challenging work for on-orbit servicing of satellites is post-capture detumbling. The objective of the post-capture phase is to detumble the rotational target satellite and stabilize the base synchronously. Accordingly, particular planning and control techniques have to be developed to cope with the challenging problem.

Many methodologies and strategies on the topic of space robot trajectory planning and motion control have been proposed in the literature. Yoshida et al. [5] employed the concept of reaction null-space (RNS)-

based reactionless manipulation to remove the time loss and the velocity limit of manipulation both for kinematically non-redundant and redundant space manipulators. Moreover, the RNS-based trajectory planning method was also applied in [6,7] to capture a tumbling target by using the momentum conservation law. Later, Xu et al. [8] presented a point-to-point path planning method using non-holonomic characteristic of free-floating space robot, while the base attitude and the end-effector's pose can be regulated synchronously. In [9], a unified singularity analysis and computation-effective avoidance method was proposed for a class of non-spherical-wrist manipulators. Lampariello et al. [10] studied the real-time trajectory planning for a robot to optimally catch a flying target, in which the desired joint trajectories were parameterized with B-splines and the Sequential Quadratic Programming (SQP) method was employed to search the optimal solution. Bézier curve was used in [11] to delineate the joint trajectory of space robot, while particle swarm optimization (PSO) method was applied to solve the optimization problem. Furthermore, Wang et al. [12] synthesized the concept of RNS and dynamic balance control in the framework of task-priority-based method to plan the motion of a kinematically redundant space robot.

For the motion control problem of space robot, Xu et al. [13] proposed an adaptive control scheme for a space robotic system with an attitude control base, whereas dynamic uncertainties were taken into account. Matsuno and Saito [14] introduced a coordinate and input transformation algorithm, which converts an affine system with a drift term into the time-state control form. Kai [15] applied model predictive control (MPC) to the attitude stabilization and the trajectory tracking control problem for a 3-dimensional universal joint space robot. Afterward, a nonlinear MPC scheme with obstacle avoidance was introduced in [16] for end-effector's path tracking. In order to achieve the best trajectory tracking for non-holonomic-wheeled mobile robots, Khooban et al. [17] introduced an optimal interval type II fuzzy proportional-integral-derivative (PID) controller with a teaching-learning-based optimization for evolving the parameters of the control. After that, Niknam et al. [18] developed a new optimal type II fuzzy sliding mode controller to control a class of uncertain nonlinear systems in the presence of external disturbances. More recently, robust control [19], sliding mode control [20], robust fuzzy sliding mode control [21], nonlinear H-infinity control [22] and robust explicit MPC [23] were also adopted in the control of multi-DOF robotic manipulators.

The aforementioned studies mainly focused on trajectory planning and motion control in the pre-capture phase. After capturing an uncontrolled satellite by a space manipulator, the target should be brought to rest as fast as possible, while the space manipulator will be demanded to apply torques to the target gently for removing any relative velocity. Nevertheless, only few studies have been investigated on the topic of optimal detumbling motion planning. In [24], a manipulator control law for the post-capture phase based on the concept of RNS was introduced to transfer angular momentum from the base toward the manipulator and to decrease the joint velocity. Yoshida et al. [25] presented a distributed momentum control method for post-capture phase, whereas the target angular momentum was transferred in the reaction wheels with minimum base attitude disturbance. An impedance control scheme has been introduced in [26] for a free-floating space robot in grasping of a tumbling target with model uncertainty. Besides, impedance control [27] was also used in dual-arm cooperative humanoid manipulators. However, optimal path planning and base attitude stabilization are not addressed in these work. In [28,29], a method for the guidance of a robotic manipulator to first intercept and then detumble a non-cooperative target satellite was introduced based on Pontryagin's minimum principle, while the minimum detumbling time was considered. A time-optimal detumbling maneuver along an arbitrary arm motion was introduced in [30] to stabilize a tumbling target satellite while paying attention to limitations on the grasping force and torque. Afterward, Abad et al. [31] designed an optimal control scheme for minimizing base attitude disturbance, in which the uncertainties in the initial and final boundary conditions were taken into account. Zhang et al. [32] derived a coordinated stabilization scenario with an adaptive sliding mode control for space robot after capturing a large inertia target.

In the previous approaches, the following shortcomings can be listed in terms of detumbling motion planning and in terms of control: (1) generally, the target motion was not generated using an optimization algorithm. Therefore, one cannot obtain an optimal solution of the detumbling motion; (2) the detumbling process for a non-cooperative target is a multi-objective, multi-constraint optimization problem, which was not considered sufficiently in the previous approaches; (3) in

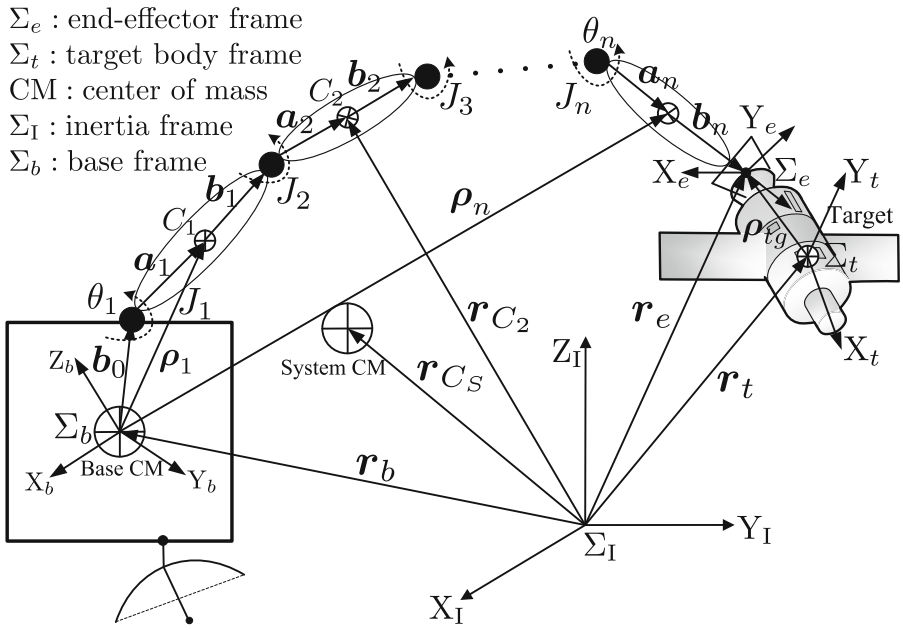

Fig. 1 Schematic diagram of space robot and target satellite

order to ensure the consistency and continuity of the end-effectors path, the detumbling motion should be continuous and smooth, which was not implemented in the previous approaches; (4) coordination controller both for the base attitude and end-effector pose was not implemented with the considering of detumbling strategy. As one can see, how to detumble the rotational motion of the target is absolutely crucial to perform further on-orbit servicing. It is noted that the design of a detumbling strategy for space manipulator is still a challenging work till nowadays.

The main motivation for this paper is to obtain a new detumbling control framework for kinematically redundant space manipulator after capturing a tumbling target satellite. The reason for choosing kinematically redundant manipulator is the existence of infinite solution which can be employed to fulfill additional constraints. Bézier curve for its simplicity and normalization is chosen to delineate the planned target's path after capturing. Moreover, constrained PSO algorithm is employed to search the optimal time and terminal pose of the target to generate the reference detumbling path for the end-effector. A coordination control scheme is derived to stabilize both space robotic base and end-effector synchronously. The original contribution of this paper is the design of the framework including optimal detumbling strategy and coordination controller for space robot in post-capture phase.

The rest of this paper is organized as follows: Sect. 2 introduces the multi-body dynamics for the combined space robotic system after capturing. An optimization-based detumbling strategy using quartic Bézier curve and constrained PSO is derived in Sect. 3. Section 4 presents a closed-form solution for coordination control of base attitude and space robotic end-effector to detumble the non-cooperative satellite. Section 5 shows the simulation results of the proposed detumbling strategy and coordination control method applied to kinematically redundant space robot. The conclusive remarks are listed in Sect. 6.

2 Dynamics after capturing

In the post-capture phase, the space manipulator and the target satellite constitutes a combined system as shown in Figs. 1 and 2. The space robotic system is composed of a spacecraft, an n DOF manipulator, in total $n+1$ bodies. Many investigations have been conducted in the field of space robot dynamics. Refer to [33–36], the dynamics equations of the space robot using Lagrangian mechanism can be expressed as follows

$$\mathbf{H}_{\mathrm{s}}\ddot{\boldsymbol{\psi}}_{\mathrm{s}} + \boldsymbol{c}_{\mathrm{s}}(\boldsymbol{\psi}_{\mathrm{s}}, \dot{\boldsymbol{\psi}}_{\mathrm{s}}) = \boldsymbol{u}_{\mathrm{s}} - \mathbf{J}_{\mathrm{se}}^{\mathrm{T}}\boldsymbol{f}_{\mathrm{e}} \tag{1}$$

where

$$\dot{\boldsymbol{\psi}}_{\mathrm{s}} \triangleq \begin{bmatrix} \dot{\boldsymbol{x}}_{\mathrm{b}} \\ \dot{\boldsymbol{\theta}}_{\mathrm{m}} \end{bmatrix}, \quad \boldsymbol{u}_{\mathrm{s}} \triangleq \begin{bmatrix} \boldsymbol{f}_{\mathrm{b}} \\ \boldsymbol{\tau}_{\mathrm{m}} \end{bmatrix}. \tag{2}$$

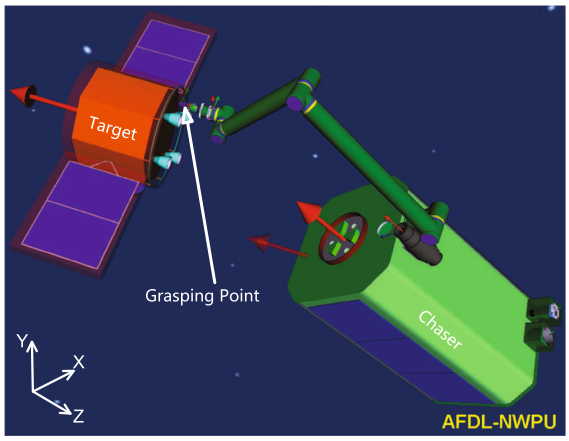

Fig. 2 Snapshot of space robot and target after capturing

$\mathbf{H}_s \in \mathbb{R}^{(n+6)\times(n+6)}$ is the generalized mass matrix of the space robotic system, $\boldsymbol{c}_s(\boldsymbol{\psi}_s, \dot{\boldsymbol{\psi}}_s) \in \mathbb{R}^{n+6}$ is generalized Coriolis and centrifugal force. $\dot{\boldsymbol{x}}_b \in \mathbb{R}^6$ represents the vector of linear and angular velocity of the base and $\dot{\boldsymbol{\theta}}_m \in \mathbb{R}^n$ is joint motion rate of manipulator. $\boldsymbol{f}_b, \boldsymbol{f}_e \in \mathbb{R}^6$ are the force and moment exert on the base and end-effector, respectively. $\boldsymbol{\tau}_m \in \mathbb{R}^n$ is the joint torque of the manipulator and $\mathbf{J}_{se} = [\mathbf{J}_b \ \ \mathbf{J}_m]$ is the Jacobian matrix with $\mathbf{J}_b \in \mathbb{R}^{6\times6}$ and $\mathbf{J}_m \in \mathbb{R}^{6\times n}$ being the Jacobian matrices for the base and for the manipulator, respectively.

The dynamics motion of the target satellite can be expressed by

$$\mathbf{H}_t\ddot{\boldsymbol{x}}_t + \boldsymbol{c}_t = \mathbf{J}_{te}^{\mathrm{T}}\boldsymbol{f}_e \tag{3}$$

where $\dot{\boldsymbol{x}}_t \in \mathbb{R}^6$ is the vector of linear velocity $\dot{\boldsymbol{r}}_t$ and angular velocity $\dot{\boldsymbol{\omega}}_t$ of the target. The generalized mass matrix $\mathbf{H}_t$ and nonlinear term $\boldsymbol{c}_t$ can be written as

$$\mathbf{H}_t = \begin{bmatrix} m_t\mathbf{E}_3 & \mathbf{0} \\ \mathbf{0} & \mathbf{I}_t \end{bmatrix}, \quad \boldsymbol{c}_t = \begin{bmatrix} m_t\boldsymbol{\omega}_t \times \dot{\boldsymbol{r}}_t \\ \boldsymbol{\omega}_t \times \mathbf{I}_t\boldsymbol{\omega}_t \end{bmatrix} \tag{4}$$

with m_t and $\mathbf{I}_t$ being the mass and inertia tensor of the targe satellite. $\mathbf{E}_3$ is an identity matrix. The grasping matrix $\mathbf{J}_{te}$ can be expressed as

$$\mathbf{J}_{te} = \begin{bmatrix} \mathbf{R}_t^e & -\tilde{\boldsymbol{\rho}}_{tg} \\ \mathbf{0} & \mathbf{R}_t^e \end{bmatrix} \tag{5}$$

$\mathbf{R}_e^t$ is the rotation matrix from end-effector's frame to target body-fixed frame and $\boldsymbol{\rho}_{tg}$ is the position vector of the grasping point with respect to the mass center of the target. For an arbitrary vector $\boldsymbol{\rho} = [\rho_x, \rho_y, \rho_z]$, $\tilde{\boldsymbol{\rho}}$ is defined as

$$\tilde{\boldsymbol{\rho}} = \begin{bmatrix} 0 & -\rho_z & \rho_y \\ \rho_z & 0 & -\rho_x \\ -\rho_y & \rho_x & 0 \end{bmatrix} \tag{6}$$

Refer to Eq. (3), the force and moment exerted by the manipulator $\boldsymbol{f}_e$ can be written as

$$\boldsymbol{f}_e = \mathbf{J}_{te}^{-\mathrm{T}}\mathbf{H}_t\ddot{\boldsymbol{x}}_t + \mathbf{J}_{te}^{-\mathrm{T}}\boldsymbol{c}_t \tag{7}$$

In post-capture phase, the velocity and acceleration relationship between the end-effector and the grasping point on the target can be established by

$$\dot{\boldsymbol{x}}_e = \mathbf{J}_{se}\dot{\boldsymbol{\psi}}_s = \mathbf{J}_{te}\dot{\boldsymbol{x}}_t \tag{8}$$

$$\ddot{\boldsymbol{x}}_e = \mathbf{J}_{se}\ddot{\boldsymbol{\psi}}_s + \dot{\mathbf{J}}_{se}\dot{\boldsymbol{\psi}}_s = \mathbf{J}_{te}\ddot{\boldsymbol{x}}_t \tag{9}$$

$$\ddot{\boldsymbol{x}}_t = \mathbf{J}_{te}^{-1}\ddot{\boldsymbol{x}}_e = \mathbf{J}_{te}^{-1}(\mathbf{J}_{se}\ddot{\boldsymbol{\psi}}_s + \dot{\mathbf{J}}_{se}\dot{\boldsymbol{\psi}}_s) \tag{10}$$

Substituting Eqs. (7) and (10) into (1) and eliminating $\boldsymbol{f}_e$, one can obtain the dynamic equation of the space robotic system after capturing a target:

$$\mathbf{H}\ddot{\boldsymbol{\psi}}_s + \boldsymbol{c}(\boldsymbol{\psi}_s, \dot{\boldsymbol{\psi}}_s) = \boldsymbol{u}_s \tag{11}$$

where

$$\mathbf{H} = \mathbf{H}_s + \mathbf{J}_{se}^{\mathrm{T}}\mathbf{J}_{te}^{-\mathrm{T}}\mathbf{H}_t\mathbf{J}_{te}^{-1}\mathbf{J}_{se}$$

$$\boldsymbol{c}(\boldsymbol{\psi}_s, \dot{\boldsymbol{\psi}}_s) = \boldsymbol{c}_s + \mathbf{J}_{se}^{\mathrm{T}}\mathbf{J}_{te}^{-\mathrm{T}}\boldsymbol{c}_t + \mathbf{J}_{se}^{\mathrm{T}}\mathbf{J}_{te}^{-\mathrm{T}}\mathbf{H}_t\dot{\mathbf{J}}_{se}\dot{\boldsymbol{\psi}}_s \tag{12}$$

3 Target detumbling strategy

Refer to Eq. (3), dynamics of the rotational motion of the target satellite can be delineated by Euler's equation as

$$\boldsymbol{\tau}_t = \mathbf{I}_t\dot{\boldsymbol{\omega}}_t + \boldsymbol{\omega}_t \times \mathbf{I}_t\boldsymbol{\omega}_t \tag{13}$$

where $\boldsymbol{\tau}_t \in \mathbb{R}^3$ is the external moments applied to the target. In pre-capture phase, it is reasonable to assume that the target satellite is free from any external forces and torques, i.e., $\ddot{\boldsymbol{r}}_t = \mathbf{0}$ and $\boldsymbol{\tau}_t = \mathbf{0}$.

As shown in Fig. 2, for a grasping point $\boldsymbol{\rho}_{tg} = [-0.35, 0, 0.4275]$ m with inertia parameters of the target satellite $\mathbf{I}_t = \mathrm{diag}(8.4, 12.18, 12.84)$ kg m^2, two simulation cases are performed with different initial angular velocities. The trajectory of the grasping point in the y–z plane of inertia frame in 5000 s is shown in Fig. 3, which indicates that the grasping point trajectory is sensitive to the initial angular velocity of the target. After capturing, the end-effector and the grasping point will coincide with zero relative velocity. Refer to Eq. (11), the rotational motion of the target satellite will continue if no detumbling strategy is applied to the target. Therefore, how to drive the target satellite from its given initial angular velocity to rest in optimal time and with minimum energy consumption is of great interest in this section.

In order to assist the design of the detumbling strategy and coordination controller, the following assumptions are presented.

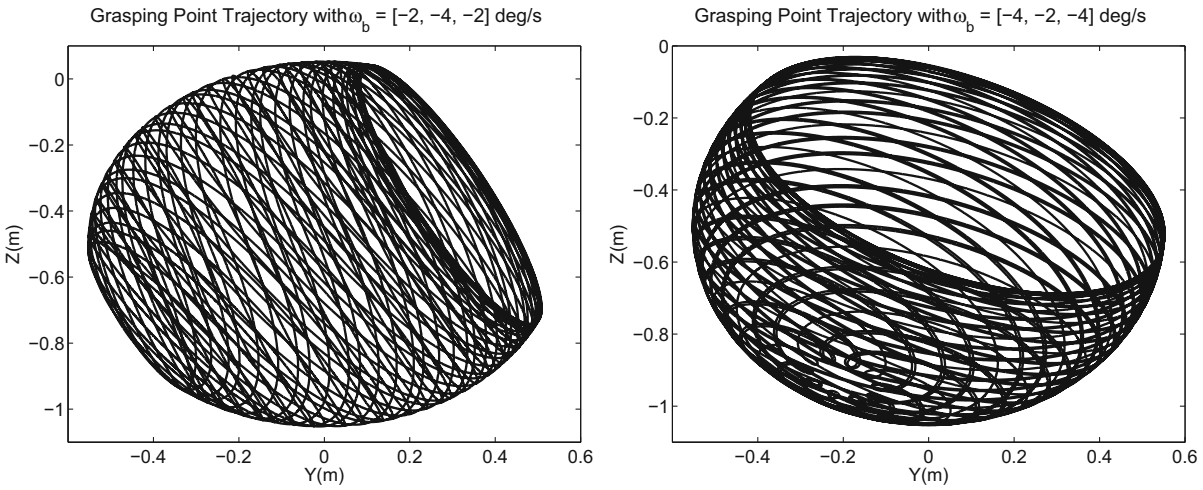

Fig. 3 Grasping point trajectory for different initial angular velocity

Assumption 1 *Vehicular operations will guide the chaser satellite (mounted with manipulator) to a necessary ready-to-capture pose with respect to the target satellite. A path tracking algorithm with an ideal visual servo tracker will align the end-effectors velocity with that of the grasping point on the target, such that the capture impact can be minimized.*

Assumption 2 *The targets body-fixed frame is located at the targets center of mass. Its mass properties can be estimated roughly from the observation* [29,30]. *The states of the target at capturing instant can be determined with provided sensors mounted on the base and manipulator.*

Assumption 3 *The mass properties parameters of the space robot (base and manipulator) can be determined accurately with parameter identification methods in pre-capture phase.*

3.1 Detumbling strategy

A detumbling strategy for a tumbling target satellite is to find an optimal path from its initial states to rest under given constraints. The initial states of the target can be determined with specified sensors, however, the terminal time and terminal states to detumble the target are still free. In this section, the target's rotational motion is expressed with Z–Y–X Euler angles $\boldsymbol{\phi} = [\alpha, \beta, \gamma]$ due to its intuitional and decoupling reasons. $\boldsymbol{\phi}$ are parameterized by Bézier curve which is widely adopted in the field of computer graphics and robotics to model smooth curves [11]. A variable with superscripts s, d and f stands for its start, desired and final value. A quartic Bézier curve ($m = 4$) is employed to describe the rotational motion of the target

$$\begin{aligned}\phi_i(\tau) &= \sum_{j=0}^{m} b_{j,m}(\tau) P_{ij} \\ &= \sum_{j=0}^{m} \binom{m}{j} (1-\tau)^{m-j} \tau^j P_{ij} \quad \tau \in [0,1] \end{aligned} \tag{14}$$

where $i = 1, 2, 3$ is the index of the Euler angles $\boldsymbol{\phi}$. The polynomials $b_{j,m}(\tau)$ are known as Bernstein basis polynomial of order m and $\binom{m}{j}$ is the binomial coefficient. P_{ij} is the given point to construct the Bézier curve. Since τ is the normalized time, for the detumbling execution time $T = t_\mathrm{f} - t_\mathrm{s}$, if we define $t = \tau \cdot T$, the target rotational motion can be calculated as follows

$$\dot{\phi}_i = \frac{\mathrm{d}\phi_i}{\mathrm{d}\tau}\frac{\mathrm{d}\tau}{\mathrm{d}t} = \frac{1}{T}\dot{\phi}_i = \frac{m}{T}\sum_{j=0}^{m-1} b_{j,m-1}(\tau)(P_{i,j+1} - P_{ij}) \tag{15}$$

$$\begin{aligned}\ddot{\phi}_i &= \frac{\mathrm{d}^2\phi_i}{\mathrm{d}\tau^2}\frac{\mathrm{d}^2\tau}{\mathrm{d}t^2} = \frac{1}{T^2}\ddot{\phi}_i \\ &= \frac{m(m-1)}{T^2}\sum_{j=0}^{m-2} b_{j,m-2}(\tau)(P_{i,j+2} - 2P_{i,j+1} + P_{ij}) \end{aligned} \tag{16}$$

The initial rotational states of the target $\boldsymbol{\phi}^\mathrm{s}$ and $\dot{\boldsymbol{\phi}}^\mathrm{s}$ can be determined at the instant of the capturing. The objec-

tive of the detumbling strategy is to make $\boldsymbol{\omega}_{\mathrm{t}}^{\mathrm{f}} = \dot{\boldsymbol{\phi}}^{\mathrm{f}} = \mathbf{0}$ and $\dot{\boldsymbol{\omega}}_{\mathrm{t}}{}^{\mathrm{f}} = \ddot{\boldsymbol{\phi}}^{\mathrm{f}} = \mathbf{0}$, which gives us four boundary conditions. As one can see, $\ddot{\boldsymbol{\phi}}^{\mathrm{s}}$ and $\boldsymbol{\phi}^{\mathrm{f}}$ are still not assigned which will be determined through optimization. Substituting the initial and final states variables into Eqs. (14), (15) and (16) and meeting the four boundary conditions $\boldsymbol{\phi}_i^{\mathrm{s}}$, $\dot{\boldsymbol{\phi}}_i^{\mathrm{s}}$, $\dot{\boldsymbol{\phi}}_i^{\mathrm{f}}$ and $\ddot{\boldsymbol{\phi}}_i^{\mathrm{f}}$

$$\begin{cases} \phi_i^{\mathrm{s}} = \phi_i(\tau = 0) = P_{i0}, \phi_i^{\mathrm{f}} = \phi_i(\tau = 1) = P_{i4} \\ \dot{\phi}_i^{\mathrm{s}} = \dot{\phi}_i(\tau = 0) = \frac{4}{T}(P_{i1} - P_{i0}), \dot{\phi}_i^{\mathrm{f}} = \dot{\phi}_i(\tau = 1) \\ \quad = \frac{4}{T}(P_{i4} - P_{i3}) \\ \ddot{\phi}_i^{\mathrm{f}} = \ddot{\phi}_i(\tau = 1) = \frac{12}{T^2}(P_{i4} - 2P_{i3} + P_{i2}) \end{cases} \tag{17}$$

From the above equations, one can derive the expression of the control point P_{ij}

$$P_{i0} = \phi_i^{\mathrm{s}}, P_{i1} = \frac{T}{4}\dot{\phi}_i^{\mathrm{s}} + \phi_i^{\mathrm{s}}, P_{i2} = \phi_i^{\mathrm{f}}, P_{i3} = \phi_i^{\mathrm{f}}, P_{i4} = \phi_i^{\mathrm{f}}. \tag{18}$$

After capturing, the angular velocity of the end-effector $\boldsymbol{\omega}_{\mathrm{e}} = \boldsymbol{\omega}_{\mathrm{t}}$. Moreover, the torques applied to the end-effector $\boldsymbol{\tau}_{\mathrm{e}} = -\boldsymbol{\tau}_{\mathrm{t}}$. In order to keep the end-effector without damage during operation, the magnitude of the torques applied to the end-effector is bounded to be below a prescribed value $\|\boldsymbol{\tau}_{\mathrm{e}}\| \leq \boldsymbol{\tau}_{\max}$. Substituting Eq. (18) into (16)

$$\begin{aligned} \ddot{\phi}_i &= \frac{12(1-\tau)}{T^2}[(P_{i2} - 2P_{i1} + P_{i0})(1-\tau) \\ &\quad + 2(P_{i3} - 2P_{i2} + P_{i1})\tau] \\ &= \frac{12(1-\tau)}{T^2} \\ &\quad \left[(\phi_i^{\mathrm{f}} - \phi_i^{\mathrm{s}} - \frac{T}{2}\dot{\phi}_i^{\mathrm{s}}) - (3\phi_i^{\mathrm{f}} - 3\phi_i^{\mathrm{s}} - T\dot{\phi}_i^{\mathrm{s}})\tau\right] \end{aligned} \tag{19}$$

The torques applied to the end-effector can be determined through $\boldsymbol{\tau}_{\mathrm{t}}$, which can be calculated using Eq. (13) with $\boldsymbol{\omega}_{\mathrm{t}} = \mathbf{J}_{\boldsymbol{\phi}}\dot{\boldsymbol{\phi}}$ and $\dot{\boldsymbol{\omega}}_{\mathrm{t}} = \dot{\mathbf{J}}_{\boldsymbol{\phi}}\dot{\boldsymbol{\phi}} + \mathbf{J}_{\boldsymbol{\phi}}\ddot{\boldsymbol{\phi}}$.

$$\mathbf{J}_{\phi} = \begin{bmatrix} 0 & -\sin\alpha & \cos\alpha\cos\beta \\ 0 & \cos\alpha & \sin\alpha\cos\beta \\ 1 & 0 & -\sin\beta \end{bmatrix},$$

$$\dot{\mathbf{J}}_{\phi} = \begin{bmatrix} 0 & -\dot{\alpha}\cos\alpha & -\dot{\alpha}\sin\alpha\cos\beta - \dot{\beta}\cos\alpha\sin\beta \\ 0 & -\dot{\alpha}\sin\alpha & \dot{\alpha}\cos\alpha\cos\beta - \dot{\beta}\sin\alpha\sin\beta \\ 0 & 0 & -\dot{\beta}\cos\beta \end{bmatrix} \tag{20}$$

Substituting the expressions of $\dot{\boldsymbol{\omega}}_{\mathrm{t}}$ and $\boldsymbol{\omega}_{\mathrm{t}}$ into Eq. (13), considering the torque constraints $\|\boldsymbol{\tau}_{\mathrm{e}}\| \leq \boldsymbol{\tau}_{\max}$, the following inequalities can be obtained

$$\begin{cases} \boldsymbol{f}_1(T) = \mathbf{I}_{\mathrm{t}}\mathbf{J}_{\phi}\ddot{\boldsymbol{\phi}} + \mathbf{I}_{\mathrm{t}}\dot{\mathbf{J}}_{\phi}\dot{\boldsymbol{\phi}} + \mathbf{J}_{\phi}\dot{\boldsymbol{\phi}} \times \mathbf{I}_{\mathrm{t}}\mathbf{J}_{\phi}\dot{\boldsymbol{\phi}} + \boldsymbol{\tau}_{\max} \geq \mathbf{0} \\ \boldsymbol{f}_2(T) = \boldsymbol{\tau}_{\max} - \mathbf{I}_{\mathrm{t}}\mathbf{J}_{\phi}\ddot{\boldsymbol{\phi}} - \mathbf{I}_{\mathrm{t}}\dot{\mathbf{J}}_{\phi}\dot{\boldsymbol{\phi}} - \mathbf{J}_{\phi}\dot{\boldsymbol{\phi}} \times \mathbf{I}_{\mathrm{t}}\mathbf{J}_{\phi}\dot{\boldsymbol{\phi}} \geq \mathbf{0} \end{cases} \tag{21}$$

Given a set of the target's terminal state $\boldsymbol{\phi}^{\mathrm{f}}$, the path for target rotation detumbling can be generated through Eqs. (14)–(18) with only one variable T. The corresponding optimal detumbling time T can be determined using binary search under prescribed constraints refer to Eq. (21):

$$T \geq \max\{T_i = \min(f_{i1}(T) \geq 0 \cap f_{i2}(T) \geq 0)\} \tag{22}$$

where $i = 1, 2, 3$ represents the index of the vectors $\boldsymbol{f}_1$ and $\boldsymbol{f}_2$.

Practically, not only the optimal detumbling time, but also the control torques applied to the target should be minimized. Therefore, during the optimization process, the following objective function is defined

$$\Gamma = w_1 T + w_2 \int_0^T \boldsymbol{\tau}_{\mathrm{t}}^{\mathrm{T}}\boldsymbol{\tau}_{\mathrm{t}}\mathrm{d}t \tag{23}$$

where $w_1, w_2 > 0$ are the weights to trade off the optimal detumbling time and control torques of the end-effector.

Consequently, define $\boldsymbol{p} = \boldsymbol{\phi}^{\mathrm{f}}$ as design variables, the detumbling strategy can be transformed to the following optimization problem which will be solved using PSO algorithm as illustrated in Sect. 3.2

$$\begin{aligned} &\min_{\boldsymbol{p}} \Gamma(\boldsymbol{p}) \\ &\text{subject to: } \|\boldsymbol{\tau}_{\mathrm{t}}(\boldsymbol{p})\| \leq \boldsymbol{\tau}_{\max}, \boldsymbol{p}_{\min} \leq \boldsymbol{p} \leq \boldsymbol{p}_{\max} \end{aligned} \tag{24}$$

where the searching region $[\boldsymbol{p}_{\min}, \boldsymbol{p}_{\max}]$ can be determined according to the initial states of the target's rotational motion. Once $\boldsymbol{p}$ is determined, the optimal detumbling time T and the target rotational motion can be solved accordingly. The required trajectories of the end-effector can be derived as follows

$$\begin{cases} \boldsymbol{q}_{\mathrm{e}}^{\mathrm{d}} = \boldsymbol{q}_{\mathrm{t}}^{\mathrm{d}} = \mathrm{Euler2quat}(\boldsymbol{\phi}) \\ \boldsymbol{\omega}_{\mathrm{e}}^{\mathrm{d}} = \boldsymbol{\omega}_{\mathrm{t}}^{\mathrm{d}} = \mathbf{J}_{\boldsymbol{\phi}}\dot{\boldsymbol{\phi}} \\ \dot{\boldsymbol{\omega}}_{\mathrm{e}}^{\mathrm{d}} = \dot{\boldsymbol{\omega}}_{\mathrm{t}}^{\mathrm{d}} = \dot{\mathbf{J}}_{\boldsymbol{\phi}}\dot{\boldsymbol{\phi}} + \mathbf{J}_{\boldsymbol{\phi}}\ddot{\boldsymbol{\phi}} \end{cases} \tag{25}$$

$$\begin{cases} \boldsymbol{r}_{\mathrm{e}}^{\mathrm{d}} = \boldsymbol{r}_{\mathrm{t}}^{\mathrm{s}} + \mathbf{R}_{\mathrm{t}}(\boldsymbol{\phi})\boldsymbol{\rho}_{\mathrm{tg}} \\ \dot{\boldsymbol{r}}_{\mathrm{e}}^{\mathrm{d}} = \dot{\boldsymbol{r}}_{\mathrm{t}}^{\mathrm{s}} + \boldsymbol{\omega}_{\mathrm{t}}^{\mathrm{d}} \times \boldsymbol{\rho}_{\mathrm{tg}} \\ \ddot{\boldsymbol{r}}_{\mathrm{e}}^{\mathrm{d}} = \ddot{\boldsymbol{r}}_{\mathrm{t}}^{\mathrm{s}} + \dot{\boldsymbol{\omega}}_{\mathrm{t}}^{\mathrm{d}} \times \boldsymbol{\rho}_{\mathrm{tg}} + \boldsymbol{\omega}_{\mathrm{t}}^{\mathrm{d}} \times (\boldsymbol{\omega}_{\mathrm{t}}^{\mathrm{d}} \times \boldsymbol{\rho}_{\mathrm{tg}}) \end{cases} \tag{26}$$

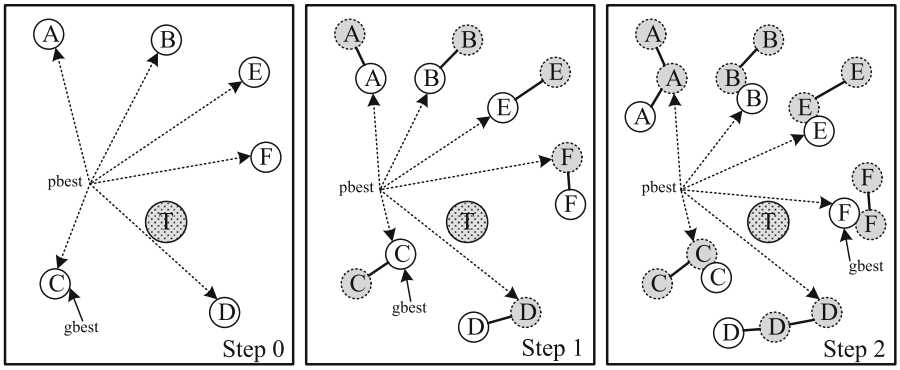

Fig. 4 Schematic diagram of PSO with 6 particles

where $\mathbf{R}_t(\boldsymbol{\phi})$ is the rotation matrix from Σ_t to Σ_I, Euler2quat($\boldsymbol{\phi}$) is a function which transforms the orientation with Euler angles into quaternion.

As one can see, the generation of the detumbling profiles is decoupled from the actual space robot that will be performing it. This decoupling is achieved through the use of $\boldsymbol{\tau}_{\max}$ in Eq. (24), since only the torque limits of the end-effector are considered in the design of the detumbling strategy. However, this requires the generated detumbling path expressed in Eqs. (25) and (26) has to be in the workspace $\mathcal{W}(\boldsymbol{\theta}_m)$ [45] of the actual space robot, which means, the generated detumbling profiles need to fulfill the constraints not only at the level of end-effector's torques, but also at the level of joint limits. The determination of the detumbling strategy can therefore be expressed as follows under the constraints of the joint limits

$$\begin{aligned} &\min_{\boldsymbol{p}} \Gamma(\boldsymbol{p}) \text{subject to: } \|\boldsymbol{\tau}_t(\boldsymbol{p})\| \leq \boldsymbol{\tau}_{\max}, \\ &\boldsymbol{p}_{\min} \leq \boldsymbol{p} \leq \boldsymbol{p}_{\max}, \boldsymbol{x}_e^d(\boldsymbol{p}) \in \mathcal{W}(\boldsymbol{\theta}_m) \end{aligned} \tag{27}$$

where $\boldsymbol{x}_e^d(\boldsymbol{p})$ is the generated detumbling path with application of Eqs. (25) and (26). The workspace $\mathcal{W}(\boldsymbol{\theta}_m)$ of the actual space robot is determined by the joint limits. As shown in Fig. 5, in order to meet the requirements of the joint limits, an additional loop is added in the optimization algorithm to check whether the designed detumbling strategy can be implemented by the actual space robot.

3.2 PSO formulations

The original PSO algorithm was inspired by the social behavior of biological organisms like flying birds, swimming fishes, etc., specially the ability of groups of some species of animals to work as a whole in locating desirable positions in a given area [38]. This seeking behavior was associated with that of an optimization search for solutions to nonlinear equations in a real-valued searching space. It is a stochastic search method but with a simpler philosophy. The main benefits of PSO [37] can be listed:

- The descent gradient of the fitness function used in traditional optimization method is not required.
- PSO is more compatible and robust compared with other classical optimization techniques.
- PSO guarantees the convergence to the optimum solution.

The PSO algorithm first initializes a population of particles with random initial values within the feasible searching space. The dimension of each particle represents the number of design variables. The states of each particle adjust in swarm taking into account the effect of stochastic, cognitive and social influence. Each particle is evaluated by the fitness function to search its own best known position (local) so far and the swarm's best known position (global) so far in the searching space. The movement of each particle is guided by the local and global best position and updated in each generation. When better positions are discovered, these will then be chosen to lead the movement of the swarm. This process is repeated by each generation until a specified condition is met or a promising solution is found. A schematic diagram of the PSO algorithm with 6 particles is shown in Fig. 4.

As illustrated in Eq.(24), the determination of the detumbling strategy is an optimization problem with multiple constraints. Suppose the swarm is composed of n_p particles, the position and velocity of the ith particle is, respectively, represented by $\boldsymbol{p}_i =$

$(p_{i1}, p_{i2}, \ldots, p_{iK})$ and $\boldsymbol{v}_i = (v_{i1}, v_{i2}, \ldots, v_{iK})$. K is the dimension of each particle. In this paper, since Euler angles were employed to delineate the target's rotation, $\boldsymbol{p}_i = \boldsymbol{\phi}^{\mathrm{f}}$ and the dimension of each particle $K = 3$. According to the principle of the PSO algorithm, the velocity and position update of the ith particle at each step can be expressed as follows

$$\begin{cases} v_{ik} = w v_{ik} + c_1 r_1 (p_{b_{ik}} - p_{ik}) + c_2 r_2 (p_{g_k} - p_{ik}) \\ x_{ik} = x_{ik} + v_{ik} \end{cases} \tag{28}$$

where w is defined as an inertia weight to control the scope of the search. c_1, c_2 are acceleration constants and r_1, r_2 are the uniformly distributed values between $[0, 1]$. $k = 1, 2, \ldots, K$ and $i = 1, 2, \ldots, n_{\mathrm{p}}$. The vector $(p_{b_{i1}}, p_{b_{i2}}, \cdots, p_{b_{iK}})$ stores the local best position of ith particle so far and $(p_{g_1}, p_{g_2}, \ldots, p_{g_K})$ represents the global best position of the swarm so far.

A widely used strategy for the inertia weight ω is to maintain a constant value over the algorithms iterations. It is shown that standard PSO [38] has a weak capability to search a fine particle due to the lack of the speed control mechanism. Refer to [39,40], by adjusting the value of ω, the swarm has a great tendency to eventually constrict itself down to the area containing the best fitness and explore that area in detail. The inertia weight w is an essential factor for the PSO efficiency which effectively controls the scope of the search [41]. In this paper, a linear decreasing strategy on w is employed

$$w = w_{\min} + \frac{\mathrm{iter}_{\max} - \mathrm{iter}}{\mathrm{iter}_{\max}} (w_{\max} - w_{\min}) \tag{29}$$

where $\mathrm{iter}_{\max}$ is the maximal number of iterations, $w_{\min}$ and $w_{\max}$ are the lower and upper bound of inertia weight, respectively. From Eq. (28), the updated velocity of ith particle is consisting of three components: a momentum of its previous velocity, velocity increments according to its local best and global best position. Eventually, the position of the particle is renewed with its previous position and new displacement is induced by the new velocity.

The so-called acceleration coefficients or control parameters c_1 and c_2 determine the relative influence of cognitive and social component for a particle's movement. Based on a convergence analysis [42], the velocity update equation in Eq. (28) can be transformed to $v_{ik} = \chi \left(v_{ik} + \varphi_1 r_1 (p_{b_{ik}} - x_{ik}) + \varphi_2 r_2 (p_{g_k} - x_{ik}) \right)$ with a constriction coefficient χ, where $\chi = \omega$ and $\chi \varphi_i = c_i$ $(i = 1, 2)$. Refer to [40], a widely used relation in PSO between c_1, c_2 and ω can be established as follows

$$\chi = \frac{2}{|2 - \varphi - \sqrt{\varphi^2 - 4\varphi}|}, \varphi = \varphi_1 + \varphi_2 \tag{30}$$

As one can see, while for $\varphi > 4$ convergence would be quick and guaranteed. For the sake of simplicity, most implementations of constricted particle swarms use equal values for both c_1 and c_2. Using the constant $\varphi = 4.1$ to ensure convergence, the values $\chi = \omega \approx 0.72984$ and $\varphi_1 = \varphi_2 = 2.05$ are obtained, which results in $c_1 = c_2 \approx 1.49617$. These values are normally used as a standard setting in the PSO algorithm.

How to choose the fitness function depends on the required space missions and the optimized objectives. In order to choose the local and global best particles in each iteration, refer to Sect. 3.1, fitness function as expressed in Eq. (23) is employed in PSO to evaluate the quality of each particle in swarm and drive them to the optimal target. Another issue that encounters in PSO is the practical constraints imposed to the design variables as illustrated in Eq. (24). Repairing infeasible solutions expressed in [43] are adopted in this paper to tackle the constraints problem.

$$p_{ik} = \begin{cases} p_{\min} & \text{if } p_{ik} < p_{\min} \\ p_{\max} & \text{if } p_{ik} > p_{\max} \\ p_{ik} & \text{otherwise} \end{cases} \tag{31}$$

Note that both position and velocity handling need to be considered in repairing strategy. If $p_{ik} < p_{\min}$ without velocity alteration, $v_{ik} < 0$ holds will drive the particle out of the feasible searching space again (similarly for $p_{ik} > p_{\max}$ and $v_{ik} > 0$). Another reason for velocity handing is the significant influence of velocity to the performance of the PSO. When it is too large, possible solution may be skipped; otherwise, if the velocity is too small, the convergence speed would be too slow. Therefore, it would make sense to set the velocity to zero or invert the kth velocity component so that the particle returns to its feasible searching region. Figure 5 shows the flowchart of the determination of target detumbling strategy using PSO algorithm. In each iteration, the fitness function is evaluated and is compared with the value computed in previous iterations. If the new value is better, new estimated values for design variables are stored. After completion of the iteration loop, the PSO with adaptive inertia weight offers an optimal solution of T^* and $\boldsymbol{p}^*$.

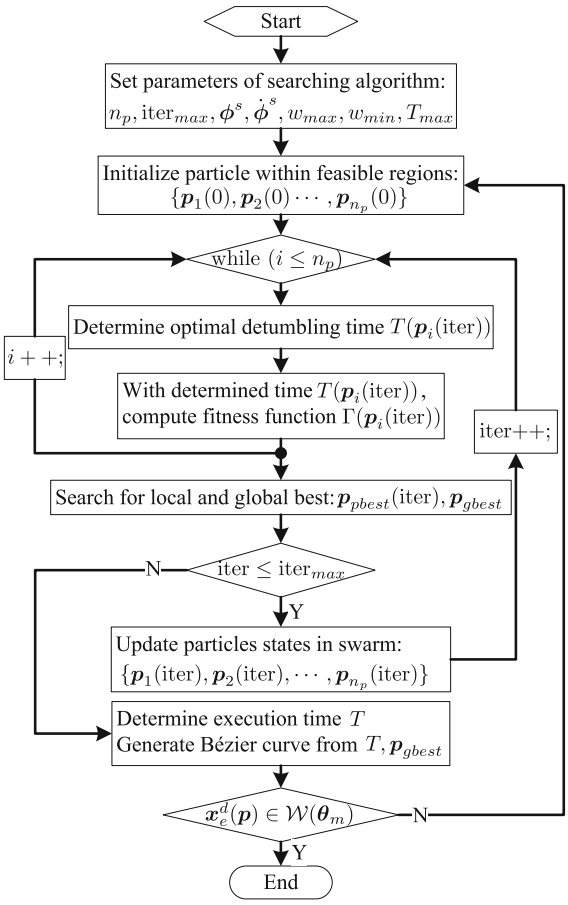

Fig. 5 The flowchart of target detumbling strategy using PSO algorithm

4 Coordination control

In order to control both base and end-effector synchronously, we are interested in writing the motion Eq. (11) in terms of the generalized velocities of the base and the end-effector, i.e., $\dot{\boldsymbol{x}}_\mathrm{b}$ and $\dot{\boldsymbol{x}}_\mathrm{e}$. Define a new velocity vector as follows

$$\dot{\boldsymbol{\psi}} \triangleq \begin{bmatrix} \dot{\boldsymbol{x}}_\mathrm{b} \\ \dot{\boldsymbol{x}}_\mathrm{e} \end{bmatrix} \tag{32}$$

Since $\mathbf{J}_\mathrm{se} = [\mathbf{J}_\mathrm{b} \ \mathbf{J}_\mathrm{m}]$, refer to Eq. (9), one can derive the joint acceleration as follows

$$\ddot{\boldsymbol{\theta}}_\mathrm{m} = \mathbf{J}_\mathrm{m}^{+}(\ddot{\boldsymbol{x}}_\mathrm{e} - \dot{\mathbf{J}}_\mathrm{se}\dot{\boldsymbol{\psi}}_\mathrm{s} - \mathbf{J}_\mathrm{b}\ddot{\boldsymbol{x}}_\mathrm{b}) \tag{33}$$

Using Eq. (33) to replace the corresponding component of $\ddot{\boldsymbol{\psi}}_\mathrm{s}$ in (11), the following dynamic equation can be obtained

$$\mathbf{D}_\mathrm{s}\ddot{\boldsymbol{\psi}} + \boldsymbol{c}_\mathrm{s}(\boldsymbol{\psi}, \dot{\boldsymbol{\psi}}) = \boldsymbol{u}_\mathrm{s} \tag{34}$$

where

$$\mathbf{D}_\mathrm{s} = \mathbf{H}\begin{bmatrix} \mathbf{E}_6 & \mathbf{0}_6 \\ -\mathbf{J}_\mathrm{m}^{+}\mathbf{J}_\mathrm{b} & \mathbf{J}_\mathrm{m}^{+} \end{bmatrix} \tag{35}$$

$$\boldsymbol{c}_\mathrm{s}(\boldsymbol{\psi}, \dot{\boldsymbol{\psi}}) = \boldsymbol{c}(\boldsymbol{\psi}_\mathrm{s}, \dot{\boldsymbol{\psi}}_\mathrm{s}) + \mathbf{H}\begin{bmatrix} \mathbf{0}_6 \\ -\mathbf{J}_\mathrm{m}^{+} \end{bmatrix}\dot{\mathbf{J}}_\mathrm{se}\dot{\boldsymbol{\psi}}_\mathrm{s} \tag{36}$$

where $\mathbf{J}_\mathrm{m}^{+}$ is the pseudo-inverse of $\mathbf{J}_\mathrm{m}$ and $\mathbf{E}_6$ is an identity matrix. Note that Eq. (34) illustrates the dynamic motion of the combined chaser and target with respect to their task-space variables. In practice, it is important to keep the base attitude unchanged in the post-capture phase for the purpose of (1) maintaining the orientation of pointing instruments and scanning devices mounted on the base; (2) reducing the collision risk during detumbling target satellite. In this paper, the translation of the base is relaxed, which means no control forces are applied to the base and the motion of the manipulator will disturb the base translation. Therefore, the generalized force input $\boldsymbol{u}_\mathrm{s}$ can be expressed as follows

$$\boldsymbol{u}_\mathrm{s} = \begin{bmatrix} \mathbf{0}_{3\times 1} \\ \bar{\boldsymbol{\tau}} \end{bmatrix} \text{ and } \bar{\boldsymbol{\tau}} = \begin{bmatrix} \boldsymbol{\tau}_\mathrm{b} \\ \boldsymbol{\tau}_\mathrm{m} \end{bmatrix} \tag{37}$$

One can derive a reduced form of the dynamic motion (34) when we define the following variables

$$\dot{\boldsymbol{\psi}} \triangleq \begin{bmatrix} \dot{\boldsymbol{r}}_\mathrm{b} \\ \dot{\bar{\boldsymbol{\psi}}} \end{bmatrix} \text{ and } \dot{\bar{\boldsymbol{\psi}}} \triangleq \begin{bmatrix} \boldsymbol{\omega}_\mathrm{b} \\ \dot{\boldsymbol{x}}_\mathrm{e} \end{bmatrix} \tag{38}$$

where $\dot{\boldsymbol{r}}_\mathrm{b}$ and $\boldsymbol{\omega}_\mathrm{b}$ represent translational and angular velocities of the base, respectively. Also, if the mass matrix $\mathbf{D}_\mathrm{s}$ and nonlinear term $\boldsymbol{c}_\mathrm{s}(\boldsymbol{\psi}, \dot{\boldsymbol{\psi}})$ can be partitioned as follows

$$\mathbf{D}_\mathrm{s} = \begin{bmatrix} \mathbf{D}_{11} & \mathbf{D}_{12} \\ \mathbf{D}_{21} & \mathbf{D}_{22} \end{bmatrix} \text{ and } \boldsymbol{c}_\mathrm{s}(\boldsymbol{\psi}, \dot{\boldsymbol{\psi}}) = \begin{bmatrix} \boldsymbol{c}_1 \\ \boldsymbol{c}_2 \end{bmatrix} \tag{39}$$

where $\mathbf{D}_{11} \in \mathbb{R}^{3\times 3}$ and $\boldsymbol{c}_1 \in \mathbb{R}^3$. The dimensions of the rest of sub-matrices and sub-vectors are consistent. The following equations can be obtained

$$\mathbf{D}_{11}\ddot{\boldsymbol{r}}_\mathrm{b} + \mathbf{D}_{12}\ddot{\bar{\boldsymbol{\psi}}} + \boldsymbol{c}_1 = \mathbf{0} \tag{40}$$

$$\bar{\mathbf{D}}\ddot{\bar{\boldsymbol{\psi}}} + \bar{\boldsymbol{c}} = \bar{\boldsymbol{\tau}} \tag{41}$$

where $\bar{\mathbf{D}}$ and $\bar{\boldsymbol{c}}$ can be derived as $\bar{\mathbf{D}} = \mathbf{D}_{22} - \mathbf{D}_{21}\mathbf{D}_{11}^{-1}\mathbf{D}_{12}$ and $\bar{\boldsymbol{c}} = \boldsymbol{c}_2 - \mathbf{D}_{21}\mathbf{D}_{11}^{-1}\boldsymbol{c}_1$.

Equation (41) shows that with proper design of torque control $\bar{\boldsymbol{\tau}}$, the base attitude and end-effector's pose could be controlled synchronously. Therefore, in order to not only track the optimal detumbling path as proposed in Sect. 3, but also to regulate the base attitude, a coordination control scheme can be obtained

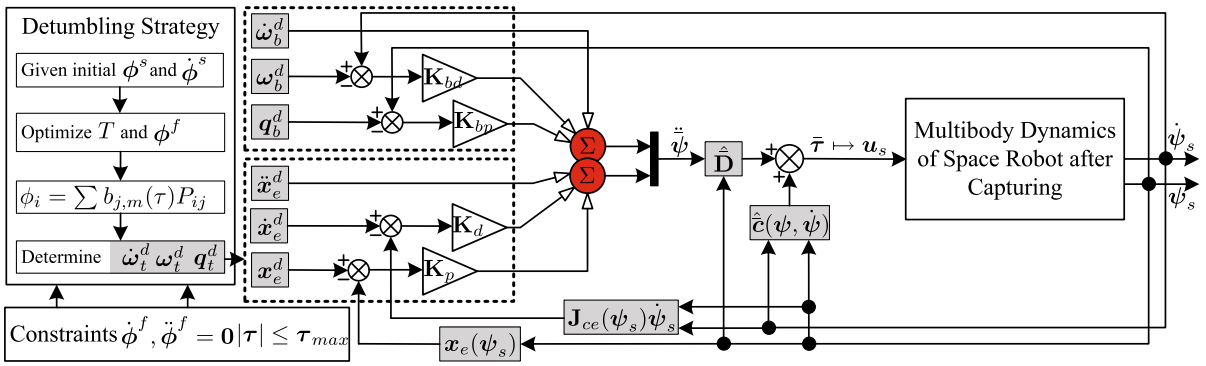

Fig. 6 Schematic diagram of coordination control for space robot after capturing

based on Eq. (41) to generate torque commands for joint motors and attitude actuators. To this end, a feedback linearization method based on dynamic model in Eq. (41) is employed to construct the coordination control scheme. The torque of coordination control for both base attitude and end-effector's pose can be calculated as

$$\bar{\boldsymbol{\tau}} = \hat{\bar{\boldsymbol{c}}} + \hat{\bar{\mathbf{D}}}\boldsymbol{y} \tag{42}$$

where $\hat{\cdot}$ represents the estimated value of a variable. Refer to [44,45], a proportion-differentiation (PD) strategy is devised for the control input $\boldsymbol{y}$ after feedback linearization:

$$\begin{aligned}\boldsymbol{y} &= \ddot{\bar{\boldsymbol{\psi}}}^{\mathrm{d}} + \mathbf{K}_{\mathrm{d}}\delta\dot{\bar{\boldsymbol{\psi}}} + \mathbf{K}_{\mathrm{p}}\delta\bar{\boldsymbol{\psi}} \\ &= \begin{bmatrix} \dot{\boldsymbol{\omega}}_{\mathrm{b}}^{\mathrm{d}} + \mathbf{K}_{\mathrm{bd}}(\boldsymbol{\omega}_{\mathrm{b}}^{\mathrm{d}} - \boldsymbol{\omega}_{\mathrm{b}}) + \mathbf{K}_{\mathrm{bp}}\delta\boldsymbol{\varepsilon}_{\mathrm{b}} \\ \ddot{\boldsymbol{r}}_{\mathrm{e}}^{\mathrm{d}} + \mathbf{K}_{\mathrm{rd}}(\dot{\boldsymbol{r}}_{\mathrm{e}}^{\mathrm{d}} - \dot{\boldsymbol{r}}_{\mathrm{e}}) + \mathbf{K}_{\mathrm{rp}}(\boldsymbol{r}_{\mathrm{e}}^{\mathrm{d}} - \boldsymbol{r}_{\mathrm{e}}) \\ \dot{\boldsymbol{\omega}}_{\mathrm{e}}^{\mathrm{d}} + \mathbf{K}_{\mathrm{ed}}(\boldsymbol{\omega}_{\mathrm{e}}^{\mathrm{d}} - \boldsymbol{\omega}_{\mathrm{e}}) + \mathbf{K}_{\mathrm{ep}}\delta\boldsymbol{\varepsilon}_{\mathrm{e}} \end{bmatrix}\end{aligned} \tag{43}$$

where $\mathbf{K}_{\cdot\mathrm{p}}$ and $\mathbf{K}_{\cdot\mathrm{d}}$ represent the feedback gains for pose and velocity, which are positive, definite matrices. Here, unit quaternion $\boldsymbol{q} = \{\eta, \boldsymbol{\varepsilon}\} \in \mathbb{R}^4$ is employed to devise the coordination control scheme (η is the scalar part, and $\boldsymbol{\varepsilon}$ is the vector part of the quaternion). The quaternion errors between $\boldsymbol{q}_1$ and $\boldsymbol{q}_2$ can be calculated as follows where $\otimes$ is the quaternion production operator

$$\begin{aligned}\{\delta\eta, \delta\boldsymbol{\varepsilon}\} &= \boldsymbol{q}_1 \otimes \boldsymbol{q}_2^{-1} \\ &= \{\eta_1\eta_2 + \boldsymbol{\varepsilon}_1^{\mathrm{T}}\boldsymbol{\varepsilon}_2, \eta_2\boldsymbol{\varepsilon}_1 - \eta_1\boldsymbol{\varepsilon}_2 - \tilde{\boldsymbol{\varepsilon}}_1\boldsymbol{\varepsilon}_2\}\end{aligned} \tag{44}$$

It is required that the base attitude is unchanged after capturing the target, i.e., $\dot{\boldsymbol{\omega}}_{\mathrm{b}}^{\mathrm{d}} = \boldsymbol{\omega}_{\mathrm{b}}^{\mathrm{d}} = \mathbf{0}$. $\boldsymbol{x}_{\mathrm{e}}^{\mathrm{d}}$, $\dot{\boldsymbol{x}}_{\mathrm{e}}^{\mathrm{d}}$ and $\ddot{\boldsymbol{x}}_{\mathrm{e}}^{\mathrm{d}}$ can be obtained from Eqs. (25) and (26). Substituting the control law in Eq. (43) into (41), one can obtain the following uncoupled differential equations

$$\delta\dot{\boldsymbol{\omega}}_{\mathrm{b}} + \mathbf{K}_{\mathrm{bd}}\delta\boldsymbol{\omega}_{\mathrm{b}} + \mathbf{K}_{\mathrm{bp}}\delta\boldsymbol{\varepsilon}_{\mathrm{b}} = \mathbf{0} \tag{45}$$

$$\delta\ddot{\boldsymbol{r}}_{\mathrm{e}} + \mathbf{K}_{\mathrm{rd}}\delta\dot{\boldsymbol{r}}_{\mathrm{e}} + \mathbf{K}_{\mathrm{rp}}\delta\boldsymbol{r}_{\mathrm{e}} = \mathbf{0} \tag{46}$$

$$\delta\dot{\boldsymbol{\omega}}_{\mathrm{e}} + \mathbf{K}_{\mathrm{ed}}\delta\boldsymbol{\omega}_{\mathrm{e}} + \mathbf{K}_{\mathrm{ep}}\delta\boldsymbol{\varepsilon}_{\mathrm{e}} = \mathbf{0} \tag{47}$$

where $\delta\dot{\boldsymbol{r}}_{\mathrm{e}} = \dot{\boldsymbol{r}}_{\mathrm{e}}^{\mathrm{d}} - \dot{\boldsymbol{r}}_{\mathrm{e}}$ and $\delta\boldsymbol{\omega} = \boldsymbol{\omega}^{\mathrm{d}} - \boldsymbol{\omega}$. Obviously, Eq. (46) is exponentially stable. Refer to [28,45], the stability of system (45) and (47) can be derived by using the Lyapunov argument:

$$V = \frac{1}{2}\delta\boldsymbol{\varepsilon}_{\mathrm{b}}^{\mathrm{T}}\mathbf{K}_{\mathrm{bp}}\delta\boldsymbol{\varepsilon}_{\mathrm{b}} + \frac{1}{2}\|\boldsymbol{\omega}_{\mathrm{b}}\|^2 \tag{48}$$

By substituting the quaternion propagation and calculating the time derivative of V:

$$\dot{V} = -\boldsymbol{\omega}_{\mathrm{b}}^{\mathrm{T}}\mathbf{K}_{\mathrm{bd}}\boldsymbol{\omega}_{\mathrm{b}} \tag{49}$$

So $\dot{V} \le 0$ for all t. Hence, global asymptotic convergence of the orientation error can be obtained. The tracking error $\delta\boldsymbol{\varepsilon}_{\mathrm{b}}$ and $\delta\boldsymbol{x}_{\mathrm{e}}$ depends on the selection of $\mathbf{K}_{\mathrm{p}}$ and $\mathbf{K}_{\mathrm{d}}$. The stability of (47) can be determined similarly. Accordingly, as $t \to \infty$, one can derive that $\boldsymbol{q}_{\mathrm{b}} \to \boldsymbol{q}_{\mathrm{b}}^{\mathrm{d}}$, $\boldsymbol{r}_{\mathrm{e}} \to \boldsymbol{r}_{\mathrm{e}}^{\mathrm{d}}$ and $\boldsymbol{q}_{\mathrm{e}} \to \boldsymbol{q}_{\mathrm{e}}^{\mathrm{d}}$. Figure 6 shows the implementation of the coordination control profile for the space robotic system in the post-capture phase.

5 Simulation results

To verify the application of the proposed detumbling strategy and coordination control method, we present an example using a kinematically redundant manipulator to capture a tumbling target in this section. As shown in Figs. 1 and 2, the chaser satellite has 6 DOF, while the manipulator is a 7-DOF arm. The kinematic and dynamic parameters of the space robot are listed in Table 1, where $\boldsymbol{a}_i$, $\boldsymbol{b}_i$ and $\mathbf{I}_i$ are expressed in its own body frame.

Table 1 Mass and inertia parameters of space robot

	Base	Link1	Link2	Link3	Link4	Link5	Link6	Link7	Target
m (kg)	200	4.0	8.0	2.0	6.0	2.0	2.0	5.0	20.0
I_{xx}	50	0.3	0.8	0.1	0.7	0.1	0.1	0.4	8.4
I_{yy}	100	0.3	0.5	0.1	0.4	0.1	0.1	0.4	12.18
I_{zz}	100	0.2	0.8	0.1	0.7	0.1	0.1	0.2	12.84
a_x (m)	0.0	0.0	0.0	0.0	0.0	0.0	0.0	0.0	–
a_y (m)	0.0	0.0	−0.7	0.0	−0.5	0.0	0.0	0.0	–
a_z (m)	0.0	0.128	0.084	0.09	0.084	0.09	0.084	0.12	–
b_x (m)	0.9	0.0	0.0	0.0	0.0	0.0	0.0	0.0	–
b_y (m)	0.084	0.084	−0.66	−0.084	−0.46	0.084	−0.09	0.0	–
b_z (m)	−0.6	0.128	0.0	0.0	0.0	0.0	0.0	0.21	–

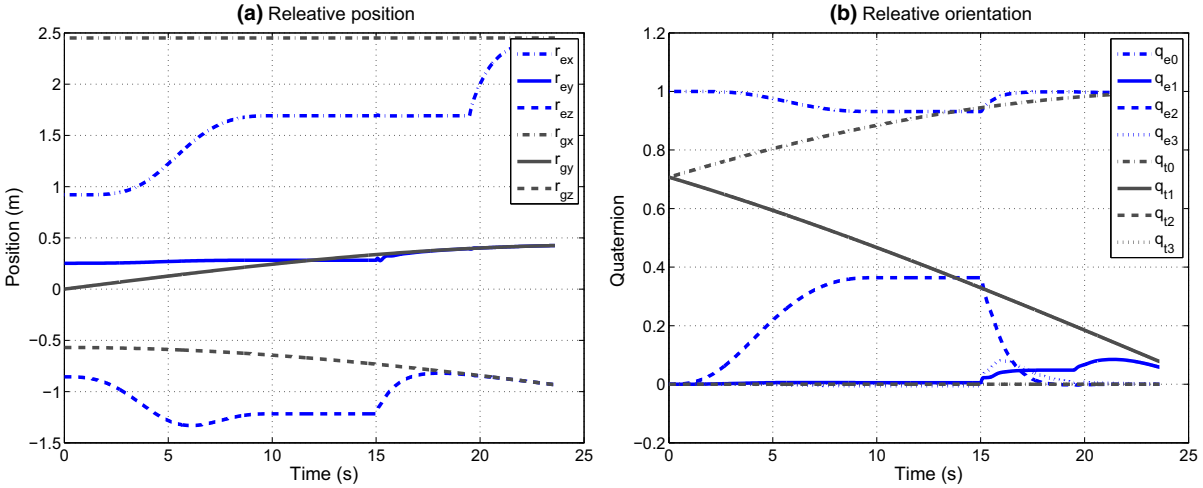

Fig. 7 Trajectories of the end-effector and grasping point in pre-capture phase

Refer to [40,42], the involved parameters of the PSO algorithm are listed as follows:

$$\begin{aligned} &n_{\mathrm{p}} = 10;\ \mathrm{iter}_{\max} = 100; \\ &c_1 = c_2 = 1.496;\ w_{\max} = 0.7298;\ w_{\min} = 0.4; \end{aligned} \tag{50}$$

With given initial states of the target, refer to Eq. (27), the determination of the detumbling strategy relies on the target mass properties estimation and the prescribed constraints. As shown in Fig. 5, the PSO algorithm first determines the optimal detumbling time T^* at each iteration, the terminal states of the target $\boldsymbol{\phi}^{\mathrm{f}}$ are optimized with fitness function expressed in Eq. (23). The detumbling path is accordingly generated.

5.1 Simulation results in pre-capture phaser

A typical process of a space robot capturing a target satellite can be roughly divided into two phases: pre-capture and post-capture. In the pre-capture phase, the manipulator moves from its home position to intercept the grasping point on the target with zero relative velocity. The grasping point is selected with $\boldsymbol{\rho}_{\mathrm{tg}} = [-0.35, 0, 0.4275]$ m expressed in target body frame. In the post-capture phase, the manipulator has to bring the target to rest under given constraints. This paper focuses on the detumbling strategy and control scheme for post-capture phase. In order to ensure consistency of the paper, Fig. 7 gives the trajectories of

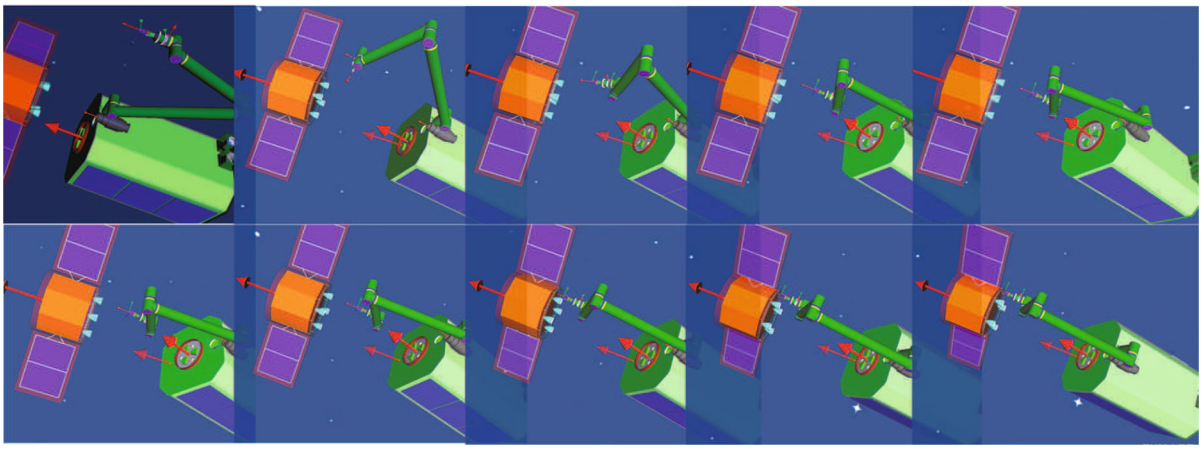

Fig. 8 Snapshot of space manipulator and target in pre-capture phase

the end-effector and the grasping point in pre-capture phase. Figure 8 shows the snapshot of the space robot and the target in the pre-capture phase.

As shown in Figs. 7 and 8, the gripper will close at $t^* = 23.60$ s when the relative pose between the end-effector's frame and grasping point's frame is small enough, which is considered that the two frames coincide. In our paper, when the relative distance and orientation are, respectively, smaller than 1 mm and 1°, it is assumed that the two frames of the end-effector and grasping point coincide and pre-capture phase ends at such an instant. A combined system is established accordingly and the detumbling strategy has to perform to rest the rotational motion of the target. At the capture moment $t^* = 23.60$ s, the states of the target and space robot are listed as follows:

$$\begin{aligned} &\boldsymbol{q}_{\mathrm{b}}^{\mathrm{s}} = (0.9547, -0.0979, 0.2807, 0.0104); \\ &\boldsymbol{\omega}_{\mathrm{b}}^{\mathrm{s}} = (3.883, -6.085, 1.467) \times 10^{-3}; \\ &\boldsymbol{\phi}_{\mathrm{t}}^{\mathrm{s}} = (0.1554, 0, 0); \dot{\boldsymbol{\phi}}_{\mathrm{t}}^{\mathrm{s}} = (-0.06, 0, 0); \end{aligned} \tag{51}$$

5.2 Coordination control simulation

Refer to [29], it is not possible to identify the absolute values of the mass parameters from observation of torque-free tumbling motion of a target satellite. Only non-dimensional inertia parameters can be obtained with scaling technique. In order to verify the effectiveness of the proposed controller, inertia parameters uncertainty is introduced into the detumbling path design as shown in Table 2. In fact, the torque constraints of the end-effector $\|\boldsymbol{\tau}_{\mathrm{e}}\| \leq \boldsymbol{\tau}_{\max}$ should not be violated for safety reasons. Therefore, it is reasonable to set the inertia parameters of the target with larger conservative values in the detumbling process. As one can see from Eq. (22), larger inertia parameters will require a longer detumbling time with bigger end-effector's internal forces and torques.

Table 2 Estimated mass properties and control gains

	m_{t} (kg)	I_{xx}	I_{yy}	I_{zz}	K_{d}	K_{p}	T^*
Nominal	20	8.4	12.18	12.84			
20% offset	24	10.08	14.616	15.408	4.0	5.0	5.1 s
50% offset	30	12.60	18.27	19.26	6.0	10.0	5.4 s

Two simulation cases with different settings in Table 2 were illustrated to analyze the performance of the proposed method. From Figs. 9 and 13, the proposed method only uses 20 or 40 iterations, which indicates that it is a fast-converging optimization. The statistical results of the proposed method were introduced to demonstrate more clearly the feasibility of the method. The implementation of the PSO was written in C and complied using the Code::Blocks complier on an i7-5600U 2.60 GHz CPU. A total of 1000 runs are performed to increase the credibility of the testing. The PSO algorithm always finds the optimal solution for the detumbling strategy and the average consumption time for each run is 0.02415 s, with higher performance CPU, the computing time will be even less.

When there are 20% uncertainties in mass properties estimation, PSO algorithm found a solution $T^* = 5.1$ s and $\boldsymbol{p}^*$= (0.1539, 0.07186, −0.0707) that fulfill all the

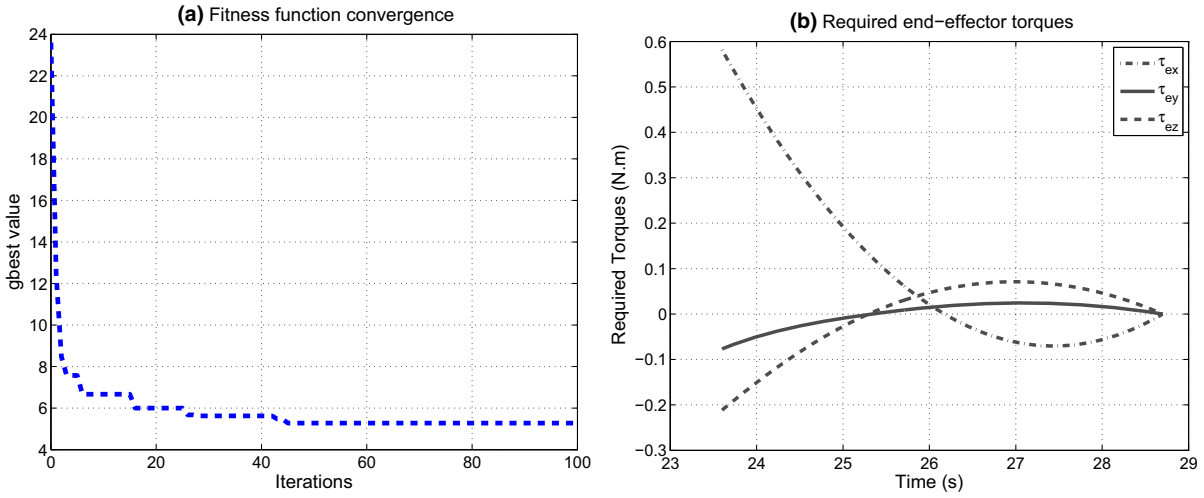

Fig. 9 Fitness evaluation and required torques with 20% target uncertainties

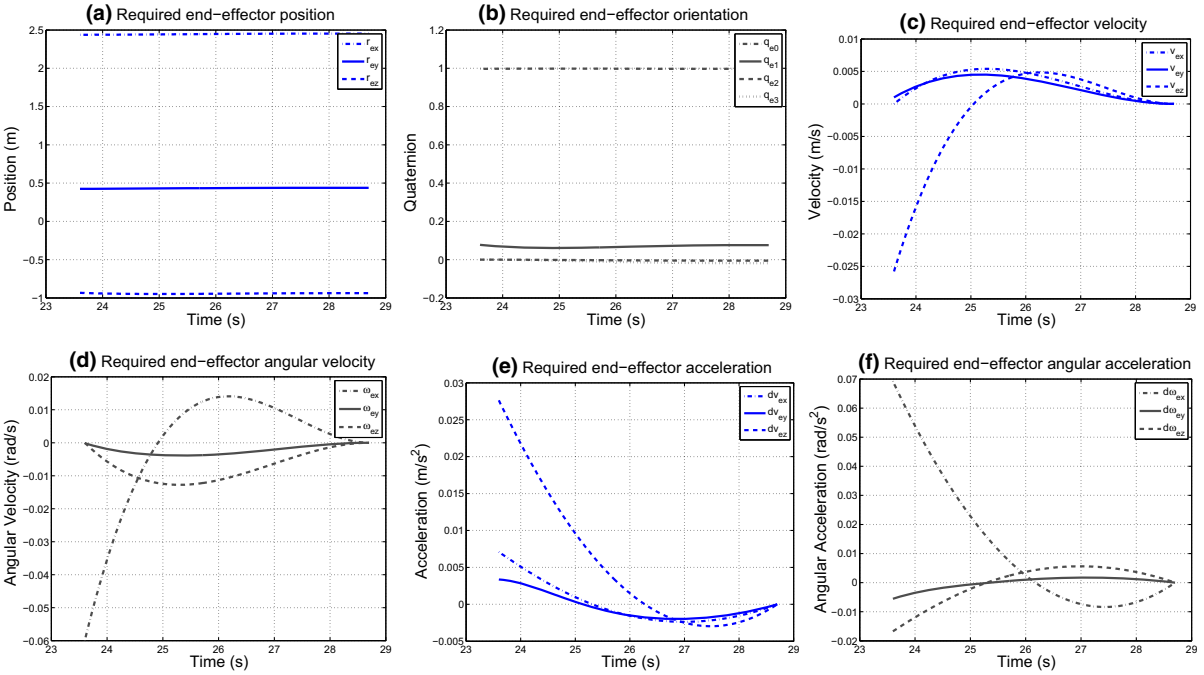

Fig. 10 Designed detumbling strategy with 20% target uncertainties

constraints. The convergence of best fitness function versus the number of iteration is shown in Fig. 9. The fitness value decreases monotonously which exhibits the searching power of the PSO algorithm. In terms of the searching solution $\boldsymbol{p}^*$ and the detumbling time T^*, the desired motion laws of the end-effector and control torques are shown in Fig. 10. One can see that with the designed detumbling strategy, the target is successfully driven to rest subject to the prescribed constraints. As shown in Fig. 9, the torque limits of the end-effector are set to $\|\tau_{i,\max}\| = 0.6\,\mathrm{N\,m}$ which will be fulfilled through adjusting the detumbling time T with Eq. (22).

Once the reference path to detumble the target is generated, the coordination control method proposed

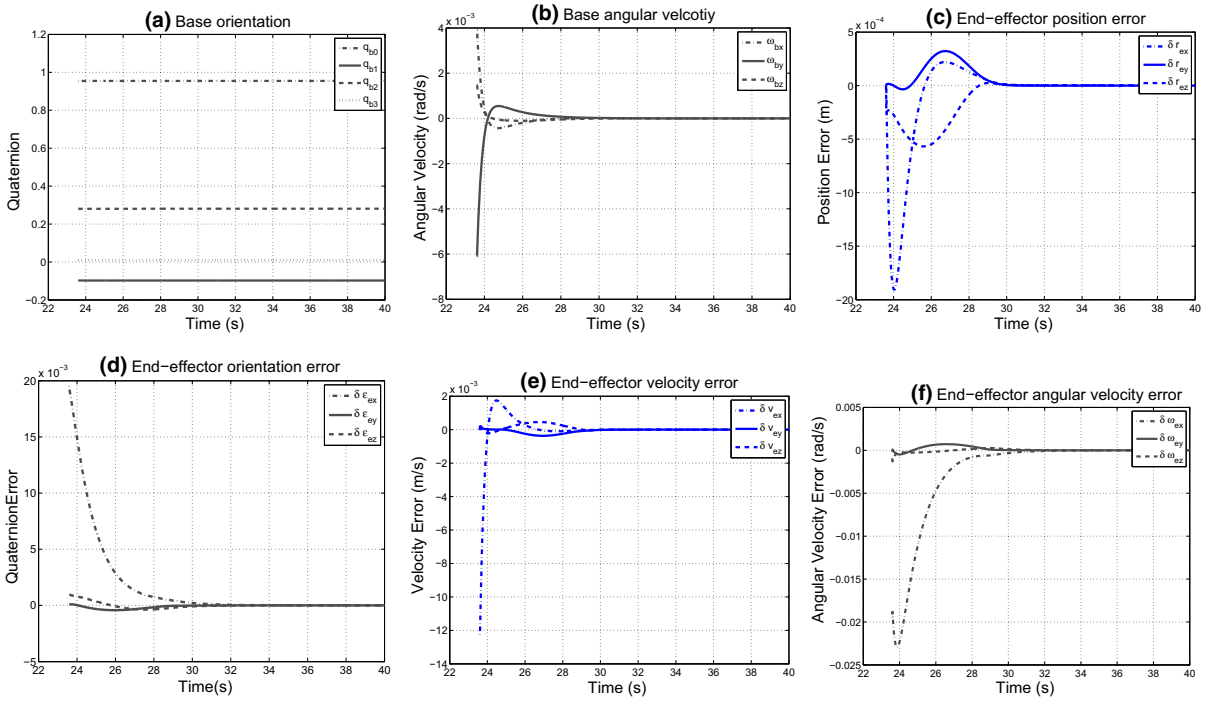

Fig. 11 Results of the coordination controller with 20% target uncertainties

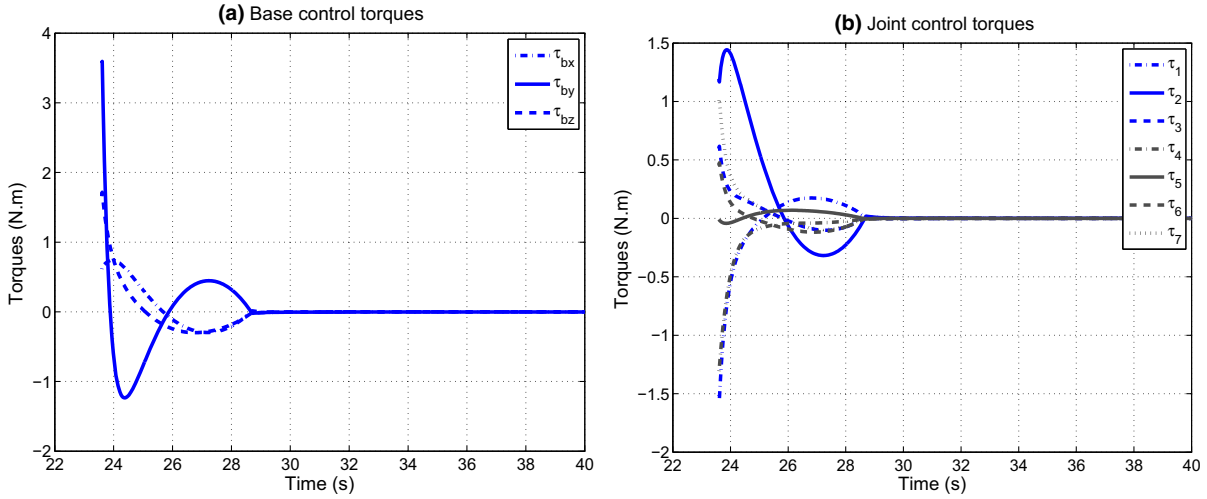

Fig. 12 Results of the control torques with 20% target uncertainties

in Sect. 4 will be applied. Refer to Eq. (43), the control gains $k_{.\mathrm{d}} = 4.0$ and $k_{.\mathrm{p}} = 5.0$ are selected for implementation of the closed-form solution. Figures 11 and 12 show the simulation results for end-effector and base attitude control. It is noted that the control procedure starts at t^* until the target was driven to rest ($\boldsymbol{\omega}_\mathrm{e} = \boldsymbol{\omega}_\mathrm{t} = \mathbf{0}$). During the detumbling process, the coordination controller tries to keep the base attitude without changing. The magnitude of the base angular velocity is less than 10^{-3} rad/s. Moreover, the controller could track the designed reference path, as well as detumble the rotational motion of the tar-

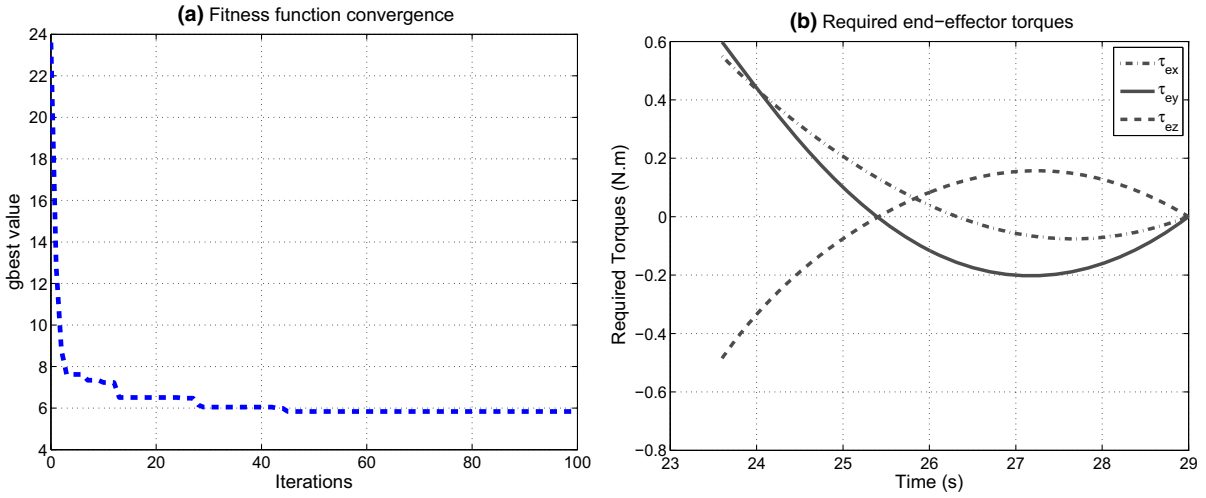

Fig. 13 Fitness evaluation and required torques with 50% target uncertainties

get. The end-effector's tracking accuracy of position $\|\delta \boldsymbol{r}_{\mathrm{e}}\| \leq 5 \times 10^{-4}$ m and orientation $\|\delta \boldsymbol{\varepsilon}_{\mathrm{e}}\| \leq 10^{-3}$, respectively. Besides, the end-effector's velocity $\dot{\boldsymbol{x}}_{\mathrm{e}}$ decreases to zero gradually, which also indicates that the rotation of the target was eliminated. One can also note that both missions for controlling end-effector's pose and base attitude were implemented. With different feedback gains, it is obvious that the coordination controller performance analysis can be represented by a second-order system $s^2 + 2\zeta\omega_{\mathrm{n}}s + \omega_{\mathrm{n}}^2 = 0$, where ζ is the damping ratio and ω_{n} is the undamped natural frequency. According to Eqs. (45)–(47), $\zeta = \frac{\mathbf{K}_{\mathrm{d}}}{2\sqrt{\mathbf{K}_{\mathrm{p}}}}$ and $\omega_{\mathrm{n}} = \sqrt{\mathbf{K}_{\mathrm{p}}}$. The transient response of the system highly relied on the selection of $\mathbf{K}_{\cdot\mathrm{p}}$ and $\mathbf{K}_{\cdot\mathrm{d}}$.

Similarly, when there are 50% uncertainties in mass properties estimation, PSO algorithm successfully found a solution $T^* = 5.4$ s and $\boldsymbol{p}^* =$(0.1525, 0.1321, -0.0722) that fulfill all the constraints. The convergence of best fitness function versus the number of iteration is shown in Fig. 13, and the desired motion laws of the end-effector and control torques are shown in Fig. 14. With large mass properties estimation, the detumbling strategy varied accordingly. Comparing Figs. 9 with 13, a longer detumbling time is required when the target mass properties estimation is with larger values.

In order to analyze the influence of the parameter selection, the control gains $k_{\cdot\mathrm{d}} = 6.0$ and $k_{\cdot\mathrm{p}} = 10.0$ are selected for implementation of the closed-form solution. The initial conditions were set as same as in Eq. (51). Figures 15 and 16 show the simulation results for end-effector pose and base attitude control. With different control gains, the transient response of the controller varied accordingly. It is noted that after detumbling the magnitude of the base angular velocity $\|\boldsymbol{\omega}_{\mathrm{b}}\| \leq 10^{-3}$ rad/s, the end-effector's tracking accuracy of position $\|\delta \boldsymbol{r}_{\mathrm{e}}\| \leq 5 \times 10^{-4}$ m and orientation $\|\delta \boldsymbol{\varepsilon}_{\mathrm{e}}\| \leq 10^{-3}$, respectively. However, it requires larger control torques both to stabilize the base and control the manipulator when compared Figs. 12 and 16. This means better estimation of the target mass properties will benefit for the design of the coordination controller. One can note that both missions for controlling end-effector's states and base attitude were successfully implemented.

In the aforementioned two simulation cases, the mass ratio between servicer and target is relatively high, which means that the target cannot heavily disturb the motion of the servicer. Additionally, the target's initial tumbling is only rotating along a single axis. In order to verify the feasibility and performance of the proposed method, another simulation case was implemented with $m_{\mathrm{t}} = 100$ kg and $\mathbf{I}_{\mathrm{t}} = \mathrm{diag}\,(18.45, 30.18, 32.84)$ kg m^2. The gripper closes at $t^* = 29.02$ s when the relative pose between the end-effector's frame and grasping point's frame is smaller than a prescribed threshold. At the capture instant $t^* = 29.02$ s, the states of the target and space robot are listed as follows:

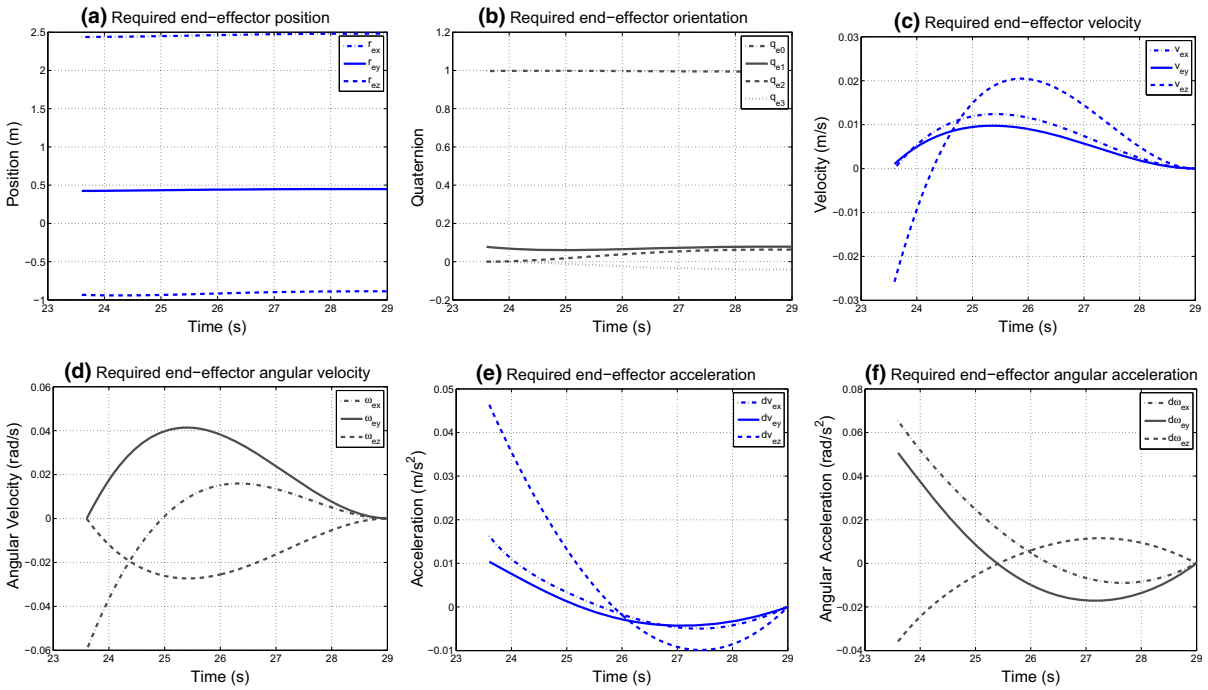

Fig. 14 Designed detumbling strategy with 50% target uncertainties

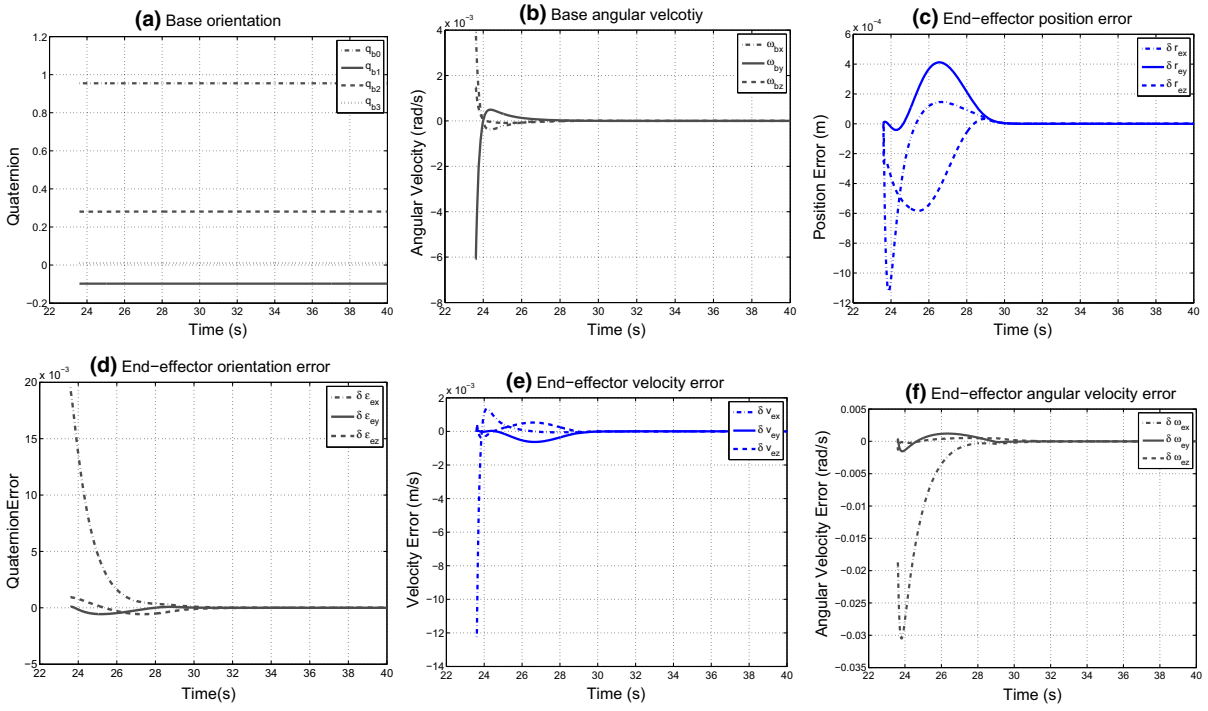

Fig. 15 Results of the coordination controller with 50% target uncertainties

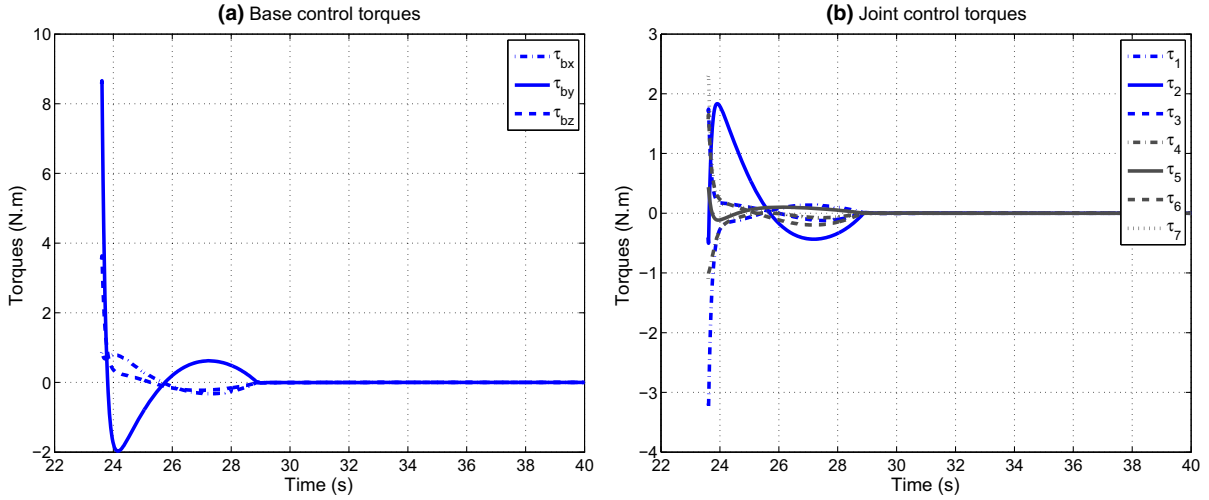

Fig. 16 Results of the control torques with 50% target uncertainties

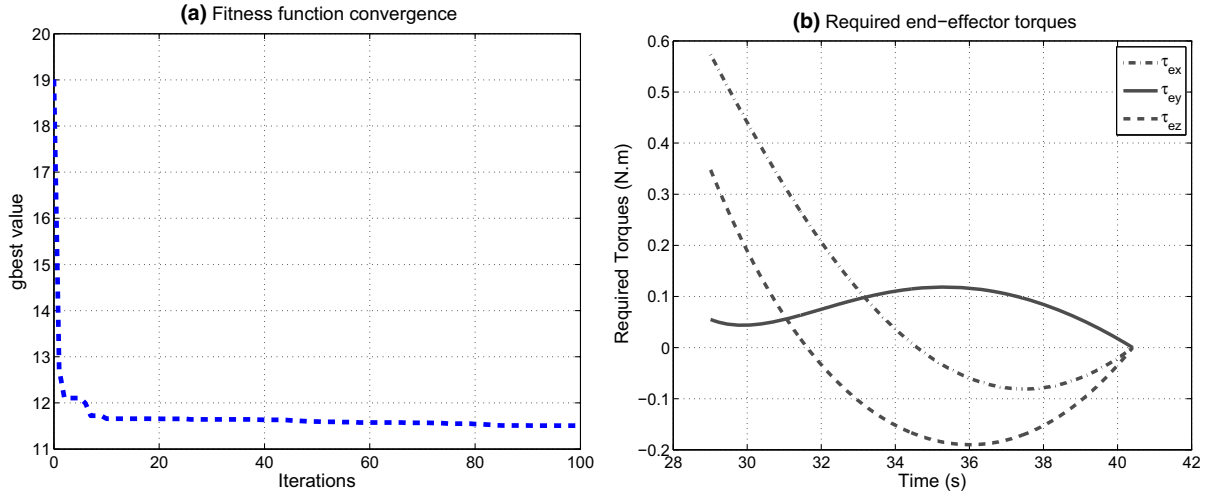

Fig. 17 Fitness evaluation and required torques with lower mass ratio

$$\begin{aligned}
\boldsymbol{q}_{\mathrm{b}}^{\mathrm{s}} &= (0.9620, 0.0647, 0.2624, 0.0393);\\
\boldsymbol{\omega}_{\mathrm{b}}^{\mathrm{s}} &= (2.000, -0.033, 5.234) \times 10^{-3};\\
\boldsymbol{\phi}_{\mathrm{t}}^{\mathrm{s}} &= (-0.1124, -0.6708, 0.3707);\\
\dot{\boldsymbol{\phi}}_{\mathrm{t}}^{\mathrm{s}} &= (-0.0786, -0.0270, 0.0325);
\end{aligned} \tag{52}$$

The torque limits of the end-effector are set to $\|\tau_{i,\max}\| = 0.6\,\mathrm{N\,m}$ as in the above simulation cases. When lower mass ratio between servicer and target was considered, PSO algorithm found a solution $T^* = 11.40\,\mathrm{s}$ and $\boldsymbol{p}^* = (-0.3373, -0.7780, 0.7278)$ that fulfill all the constraints. The determination of the detumbling time T was derived with Eq. (22). The convergence of the best fitness function versus the number of iteration is shown in Fig. 17. In terms of the determined optimal solution $\boldsymbol{p}^*$ and the detumbling time T^*, the desired motion laws of the end-effector and control torques are shown in Fig. 18.

With the generated detumbling path as shown in Fig. 18, the coordination control method proposed in Sect. 4 will be applied to stabilize the whole space robotic system. Refer to Eq. (43), the control gains $k_{.\mathrm{d}} = 4.0$ and $k_{.\mathrm{p}} = 6.0$ are selected for implementation of the closed-form solution. Figures 19 and 20 show the simulation results for end-effector and base attitude control when lower mass ratio between servicer and target was considered. The control procedure begins at t^* until the target was driven to rest ($\boldsymbol{\omega}_{\mathrm{e}} =$

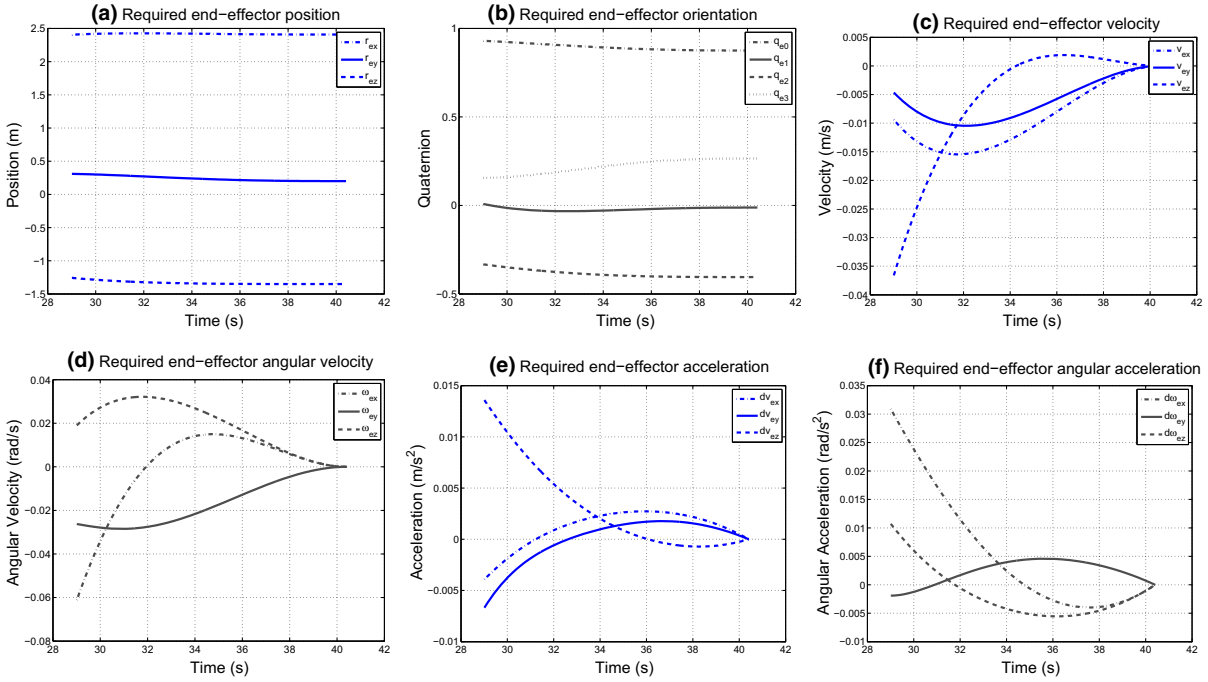

Fig. 18 Designed detumbling strategy with lower mass ratio

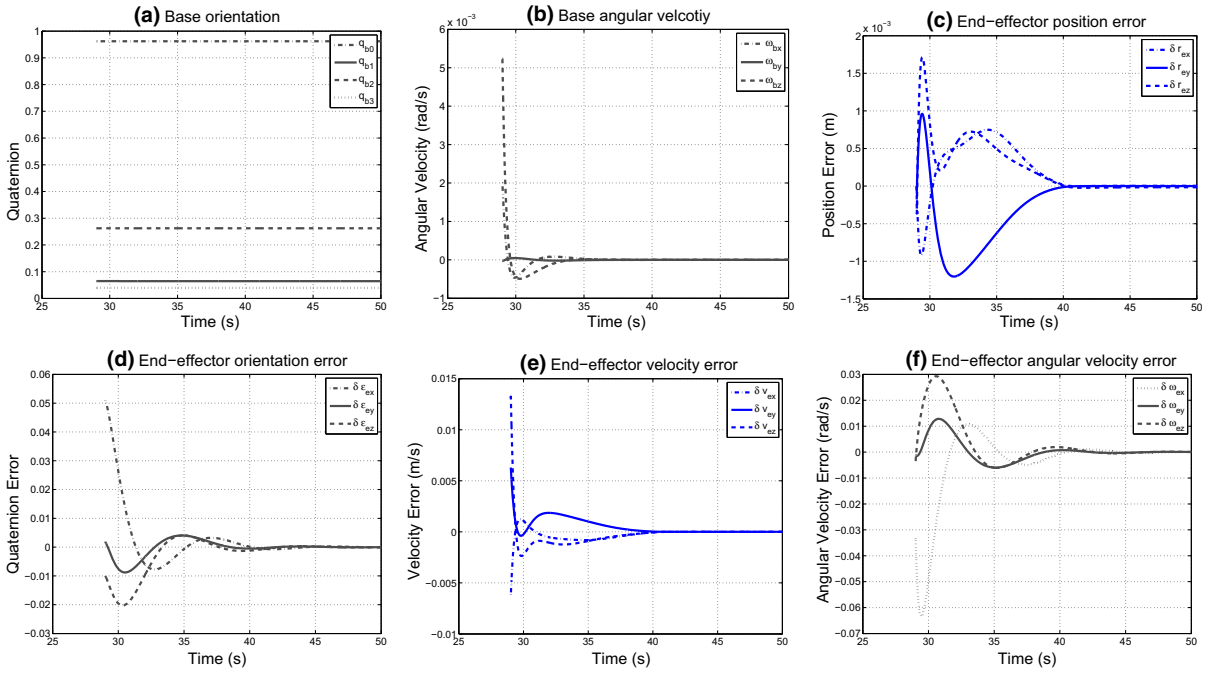

Fig. 19 Results of the coordination controller with lower mass ratio

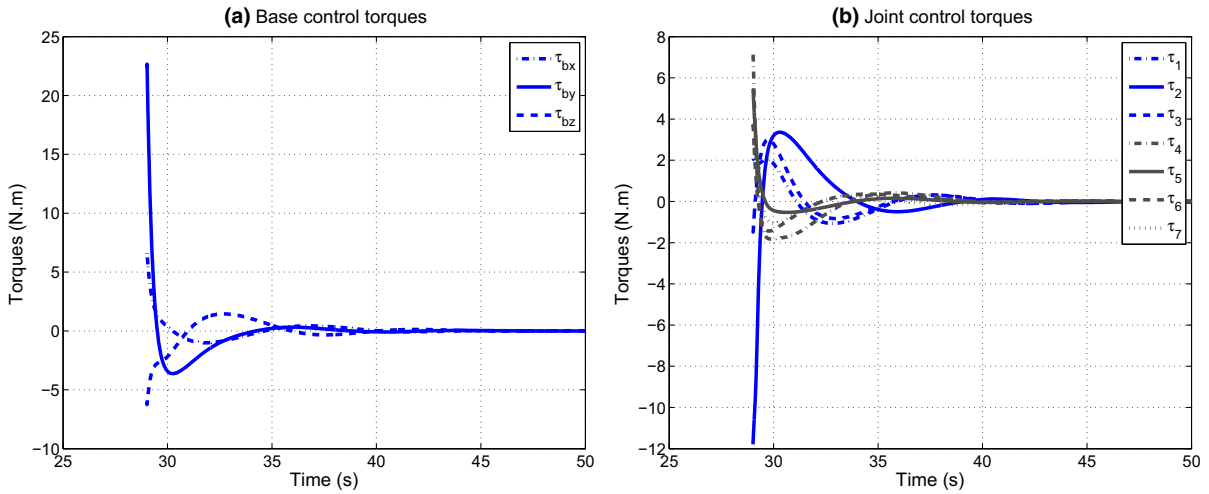

Fig. 20 Results of the control torques with lower mass ratio

$\boldsymbol{\omega}_t = \mathbf{0}$). During the detumbling process, the coordination controller tries to keep the base attitude without changing. The magnitude of the base angular velocity is less than 10^{-3} rad/s. Furthermore, the controller could track the designed reference path, as well as detumble the rotational motion of the target. The end-effector's tracking accuracy of position $\|\delta \boldsymbol{r}_e\| \leq 2 \times 10^{-3}$ m and orientation $\|\delta \boldsymbol{\varepsilon}_e\| \leq 10^{-2}$, respectively. Besides, the end-effector's velocity $\dot{\boldsymbol{x}}_e$ decreases to zero gradually, which also implies that the rotation of the target was eliminated. One can also note that both missions for controlling end-effector's pose and base attitude were implemented. However, refer to Figs. 18 and 20, when lower mass ratio between servicer and target was considered, it is reasonable to obtain a longer detumbling duration with the prescribed end-effector's torque limits. Besides, larger control torques both for base and joint actuators were required to detumble and stabilize the space robotic system. Conclusively, the designed detumbling strategy and coordination control scheme are applicable and effective to perform satellite grasping missions with application of space robot.

6 Conclusions

In post-capture phase, in order to drive a tumbling target satellite to rest as soon as possible and with minimum time and control torques, an optimal detumbling strategy and coordination control scheme for space robot have been presented. The main features of this paper can be listed as follows:

1. The dynamic equations for kinematically redundant space robot after capturing a non-cooperative target satellite was derived in terms of generalized velocities of the base and end-effector, which lays a foundation for the controller design.
2. Quartic Bézier curves are employed to delineate the detumbling path and constrained particle swarm optimization (PSO) with adaptive inertia weight is applied to search the optimal terminal states subject to prescribed constraints. Both detumbling time and control torques are considered during the optimization.
3. A coordination control scheme was developed to detumble the target rotational motion and regulate base attitude synchronously.

The proposed method in this paper successfully dumps the initial rotational velocity of the tumbling target and stabilize the base attitude in the post-capture phase. The ability and effectiveness of the detumbling strategy and coordination controller was demonstrated by simulation results. Robust coordination controller design in uncertain knowledge of measurements and parameters will be addressed in our future work.

Acknowledgements This research was supported by "the National Natural Science Foundation of China (Grant No. 61603304, 61690210)" and "Shenzhen Future Industry Special Fund (Grant No. JCYJ20160531174213774)."

References

1. Hirzinger, G., Brunner, B., Dietrich, J., Heindl, J.: ROTEX—the first remotely controlled robot in space. In: Proceedings of the IEEE Conference on Robotics and Automation, pp. 2604–2611. San Diego, CA (1994)
2. Inaba, N., Oda, M.: Autonomous satellite capture by a space robot. In: Proceedings of the IEEE Conference on Robotics and Automation, pp. 1169–1174. San Francisco, CA (2000)
3. Ogilvie, A., Allport, J., Hannah, M., Lymer, J.: Autonomous satellite servicing using the orbital express demonstration manipulator system. In: Proceedings of the 9th International Symposium on Artificial Intelligence, Robotics and Automation in Space, iSAIRAS, pp. 25–29. Los Angeles, CA (2008)
4. Rekleitis, I., Martin, E., Rouleau, G., L'Archeveque, R., Parsa, K., Dupuis, E.: Autonomous capture of a tumbling satellite. J. Field Robot. **23**, 275–296 (2007)
5. Yoshida, K., Hashizume, K., Abiko, S.: Zeros reaction maneuver: flight validation with ETS-VII space robot and extension to kinematically redundant arm. In: Proceedings of the IEEE Conference on Robotics and Automation, pp. 441–446. Seoul, Korea (2001)
6. Nguyen-Huynh, T., Sharf, I.: Adaptive reactionless motion for space manipulator when capturing an unknown tumbling target In: Proceedings of the IEEE Conference on Robotics and Automation, pp. 4202–4207. Shanghai, China (2011)
7. Shah, S., Sharf, I., Misra, A.: Reactionless path planning strategies for capture of tumbling objects in space using a dual-arm robotic system. In: AIAA Conference on Guidance, Navigation, and Control, Boston, MA (2013)
8. Xu, W., Li, C., Wang, X., Liang, B.: Study on non-holonomic cartesian path planning of a free-floating space robotic system. Adv. Robot. **23**(1–2), 113–143 (2009)
9. Xu, W., Zhang, J., Liang, B., Li, B.: Singularity analysis and avoidance for robot manipulators with non-spherical wrist. IEEE Trans. Ind. Electron. **63**(1), 277–290 (2016)
10. Lampariello, R., Tuong, D., Castellini, C., Hirzinger, G., Peters, J.: Trajectory planning for optimal robot catching in real-time. In: Proceedings of the IEEE Conference on Robotics and Automation, pp. 3719–3726. Shanghai, China (2011)
11. Wang, M., Luo, J., Walter, U.: Trajectory planning of free-floating space robot using particle swarm optimization (PSO). Acta Astronaut. **112**, 77–88 (2015)
12. Wang, M., Luo, J., Walter, U.: Novel synthesis method for minimizing attitude disturbance of the free-floating space robots. J. Guid. Control Dyn. **39**(3), 695–704 (2016)
13. Xu, Y., Shum, H., Lee, J., Kanade, T.: Adaptive control of space robot system with an attitude controlled base. In: Proceedings of the IEEE Conference on Robotics and Automation, pp. 2005–2010. Nice, France (1992)
14. Matsuno, F., Saito, K.: Attitude control of a space robot with initial angular momentum. In: Proceedings of the IEEE Conference on Robotics and Automation, pp. 1400–1405. Seoul, Korea (2001)
15. Kai, T.: A Model predictive control approach to attitude stabilization and trajectory tracking control of 3D universal joint space with an initial angular momentum. In: Proceedings of the IEEE Conference on Decision and Control, pp. 3547–3552. St. Orlando, FL (2011)
16. Wang, M., Luo, J., Walter, U.: A non-linear model predictive control with obstacle avoidance for a space robot. Adv. Space Res. **57**(8), 1737–1746 (2016)
17. Khooban, M., Alfi, A., Abadi, D.: Teaching-learning-based optimal interval type-2 fuzzy PID controller design: a nonholonomic wheeled mobile robots. Robotica **31**(7), 1059–1071 (2013)
18. Niknam, T., Khooban, M., Kavousifard, A., Soltanpour, M.: An optimal type II fuzzy sliding mode control design for a class of nonlinear systems. Nonlinear Dyn. **75**, 73–83 (2014)
19. Pan, H., Xin, M.: Nonlinear robust and optimal control of robot manipulators. Nonlinear Dyn. **76**, 237–254 (2014)
20. Zadeh, S., Khorashadizadeh, S., Fateh, M., Hadadzarif, M.: Optimal sliding mode control of a robot manipulator under uncertainty using PSO. Nonlinear Dyn. **84**, 2227–2239 (2016)
21. Soltanpour, M., Khooban, M., Soltani, M.: Robust fuzzy sliding mode control for tracking the robot manipulator in joint space and in presence of uncertainties. Robotica **32**(3), 433–446 (2014)
22. Rigatos, G., Siano, P., Raffo, G.: A nonlinear h-infinity control method for multi-DOF robotic manipulators. Nonliear Dyn. **88**, 329–348 (2017)
23. Wei, C., Luo, J., Dai, H., Yin, Z., Ma, W., Yuan, J.: Globally robust explicit model predictive control of constrained systems exploiting SVM-based approximation. Int. J. Robust Nonlinear Control **27**, 3000–3027 (2017)
24. Nenchev, D., Yoshida, K.: Impact analysis and post-impact motion control issue of a free-floating space robot subject to a force impulse. IEEE Trans. Robot. Autom. **15**, 548–557 (1999)
25. Yoshida, K., Dimitrov, D., Nakanishi, H.: On the capture of tumbling satellite by a space robot. In: Proceedings of the IEEE/RSJ Conference on Intelligent Robots and Systems, pp. 4127–4132. Beijing, China (2006)
26. Abiko, S., Lampariello, R., Hirzinger, G.: Impedance control for a free-floating robot in the grasping of a tumbling target with parameter uncertainty. In: Proceedings IEEE/RSJ Conference on Intelligent Robots and Systems, pp. 1020–1025. Beijing, China (2006)
27. Ren, Y., Zhou, Y., Liu, Y., Jin, M., Liu, H.: Adaptive objective impedance control of dual-arm cooperative humanoid manipulators. In: Proceedings of the 11th World Conference on Intelligent Control and Automation, pp. 3333–3339. Shenyang, China (2014)
28. Aghili, F.: Coordination control of a free-flying manipulator and its base attitude to capture and detumble a noncooperative satellite. In: Proceedings of the IEEE/RSJ Conference on Intelligent Robots and Systems, pp. 2365–2372. St. Louis, MO (2009)
29. Aghili, F.: A prediction and motion-planning scheme for visually guided robotic capturing of free-floating tumbling objects with uncertain dynamics. IEEE Trans. Robot. **28**(3), 634–649 (2012)
30. Oki, T., Abiko, S., Nakanishi, H., Yoshida, K.: Time-optimal detumbling maneuver along an arbitrary arm motion during the capture of a target satellite. In: Proceedings IEEE/RSJ Conference on Intelligent Robots and Systems, pp. 625–630. San Francisco, CA (2011)

31. Flores-Abad, A., Zhang, L., Wei, Z., Ma, O.: Optimal capture of a tumbling object in orbit using a space manipulator. J. Intell. Robot. Syst. **86**, 199–211 (2017)
32. Zhang, B., Liang, B., Wang, Z., Mi, Y., Zhang, Y., Chen, Z.: Coordinated stabilization for space robot after capturing a noncooperative target with large inertia. Acta Astronaut. **134**, 75–84 (2017)
33. Agrawal, S., Garimella, R., Desmier, G.: Free-floating closed-chain planar robots: kinematics and path planning. Nonlinear Dyn. **9**, 1–19 (1996)
34. Cyril, X., Misra, A., Ingham, M., Jaar, G.: Postcapture dynamics of a spacecraft-manipulator-payload system. J. Guid. Control Dyn. **23**, 95–100 (2000)
35. Wang, M., Walter, U.: Joint-space dynamics algorithm for tree structure space manipulators by using inertia mapping matrix. In: Proceedings ECCOMAS Thematic Conference on Multibody Dynamics, pp. 819–829. Zagreb, Croatia (2013)
36. Xu, W., Peng, J., Liang, B., Mu, Z.: Hybrid modeling and analysis method for dynamic coupling of space robots. IEEE Trans. Aerosp. Electron. Syst. **52**(1), 85–98 (2016)
37. Soltanpour, M., Khooban, M.: A particle swarm optimization approach for fuzzy sliding mode control for tracking the robot manipulator. Nonlinear Dyn. **74**, 467–478 (2013)
38. Clerc, M., Kennedy, J.: The particle swarm explosion, stability, and convergence in a multidimensional complex space. IEEE Trans. Evol. Comput. **6**(1), 58–73 (2002)
39. Shi, Y., Everhart, R.: Parameter selection in particle swarm optimization. In: Proceedings of the 7th Conference on Evolutionary Programming VII, pp. 591–600. San Diego, CA (1998)
40. Bratton, D., Kennedy, J.: Defining a standard for particle swarm optimization. In: Proceedings IEEE Swarm Intelligence Symposium, pp. 120–127. Honolulu, HI (2007)
41. Kentzoglanakis, K., Poole, M.: Particle swarm optimization with an oscillating inertia weight. In: Proceedings of the 11th Annual Conference on Genetic and Evolutionary Computation, pp. 1749–1750. Montreal, Canada (2009)
42. Trelea, I.: The particle swarm optimization algorithm: convergence analysis and parameter selection. Inform. Process. Lett. **85**, 317–325 (2003)
43. Helwig, S.: Particle swarms for constrained optimization. Doctoral diss, Erlangen University, Erlangen, Germany (2010)
44. Chiaverini, S.: Singularity-robust task-priority redundancy resolution for real-time kinematic control of robot manipulators. IEEE Trans. Robot. Autom. **13**, 398–410 (1997)
45. Siciliano, B., Sciavicco, L., Villani, L., Oriolo, G.: Robotics modelling, planning and control, 1st edn. Springer, London (2009)